PROCEEDINGS OF THE SCHOOL OF ENGINEERING OF TOKAI UNIVERSITY

SERIES E.

VOL. 51, 2026

C O N T E N T S

Technical Papers

Proc. Schl. Eng. Tokai Univ., Ser. E
51 (2026) 1-5
DOI: 10.18995/24343641. 51. 1

Analysis on the Membrane Topology and Self-Interaction of Yeast Alg7p

by

Shuo CUI*1, Yedan ZHOU*2 and Tetsuo TAKAHASHI*3

(Received on Apr. 7, 2026 and accepted on Jun. 16, 2026)

Abstract

In the first stage of assembly of dolichol-linked oligosaccharide (DLO), yeast Alg7p transfers *N*-acetylglucosamine-1-phosphate (GlcNAc-1-P) from UDP-GlcNAc to dolichol phosphate (Dol-P). In this study, we cloned the *ALG7* gene, which encodes yeast GlcNAc-1-P transferase, Alg7p, and analyzed the membrane topology and physical interaction of Alg7p, using the yeast split-ubiquitin system (YSUS). Our research revealed that Alg7p has at least four transmembrane domains (TMDs) with both termini oriented toward the cytoplasmic side of the rough ER (rER) membrane. In addition, it was revealed that Alg7p physically interacts with itself, suggesting that it might function in the form of a homodimer.

Keywords: GlcNAc-1-P transferase, Membrane topology, Physical interaction, Split-ubiquitin system

1. Introduction

In eukaryotes, biosynthesis of dolichol-linked oligosaccharides (DLOs) is essential for the protein *N*-glycosylation within the rough endoplasmic reticulum (rER). In the assembly of DLO on the rER membrane, the *N*-acetylglucosamine-1-phosphate (GlcNAc-1-P) transferase (GPT) utilizes dolichol phosphate (Dol-P) and UDP-GlcNAc to produce the shortest DLO, GlcNAc-PP-dolichol[1]. In budding yeast, the gene encoding the GPT were originally identified as a tunicamycin-resistant gene[2], and isolated as the *ALG7* gene[3]. Thereafter, orthologous GPT genes have been cloned in hamster[4], mouse[5] and human[6].

In order to investigate the membrane topology and physical interaction of enzymes which are localized on the ER membrane and involved in DLO assembly, we have been utilizing the yeast split-ubiquitin system (YSUS)[7-10], which has so far identified the physical interaction of various membrane proteins with other membrane proteins[11-25]. Recently, we successfully characterized the membrane topology and physical interaction of human GPT (hGPT)[19]. Therefore, we investigated those of yeast Alg7p using the YSUS.

2. Experimental Methods

2.1 *Prediction of the membrane topology of Alg7p*

Firstly, we predicted the membrane topology of Alg7p using a TOPCONS WWW algorithm server[26], (https://topcons. cbr.su.se). On its WEB site, the amino acid sequence of Alg7p consisting of 448 residues was registered and surveyed about its potential transmembrane domains (TMDs) and membrane topology.

2.2 *Construction of recombinant plasmids for the YSUS*

The coding region of *ALG7* gene was amplified from genomic DNA derived from *Saccharomyces cerevisiae* NMY51 strain by standard PCR method[27] using AG7BPfw and AG7BPrv primers listed in Table 1. A PCR product was then digested with *Sfi* I, purified and ligated to the pBT-N or pBT-STE plasmid vector for expression of Alg7p bait protein which has Cub (*C*-terminal half of ubiquitin protein) tag prepared in the YSUS, at the *N*- or *C*- terminus, respectively. Subsequently, the ligation mix was used for transformation of *Escherichia coli* JM109 strain prepared by SEM method[28]. Preparation of each recombinant plasmid from the transformants was conducted by standard cloning method[29], generating pBT-N-AG7 and pBT-STE-AG7 bait constructs (Fig. 2).

In order to analyze membrane topology of Alg7p, nine pBT-STE-based constructs (pBT-STE-AG7/LR2 to pBT-STE-AG7/LR10) for expression of the *C*-terminally truncated Alg7p bait proteins in yeast were prepared via PCR cloning described above (Fig. 2).

In order to analyze the physical interaction of Alg7p, the prey constructs (pPR-N-AG7 and pPR-STE-AG7) that would express Alg7p prey protein having Nub G (*N*-terminal half of I13G mutational ubiquitin protein) tag at the *N*- or *C*-terminus, were also prepared by the same procedure, except usage of the pPR-N and pPR-STE plasmid vectors instead of

*1 Graduate Student, Course of Applied Science and Chemistry
*2 Undergraduate Student, Department of Bioengineering
*3 Associate Professor, Department of Bioengineering

Table I The PCR primers used in this study. Additional sequences containing a *Sfi* I- cleavage site are shown in lowercase letters.

Primer name	Nucleotide sequence	Purpose
AG7BPfw	5'-tgtaatggccattacggccATGTTGCGACTTTTTTCACTGG-3'	Cloning of full-length and truncated *ALG7*
AG7BPrv	5'-gcctttggccgaggcggccCAACGTACTGTCCATAGGTTGTCG-3'	Cloning of full-length *ALG7*
AG7PSTfw	5'-gtcagtggccattacggcccgATGTTGCGACTTTTTTCACTGG-3'	Cloning of full-length *ALG7* into pPR-STE vector
AG7(LR2)BPrv	5'-gcctttggccgaggcggccGTTTCTGGAAGCACCGGACGGC-3'	Cloning of truncated *ALG7* from *N*-terminus to LR2
AG7(LR3)BPrv	5'-gcctttggccgaggcggccttATCATGAGGAAAAATATTAGAATTCATAC-3'	Cloning of truncated *ALG7* from *N*-terminus to LR3
AG7(LR4)BPrv	5'-gcctttggccgaggcggccCTTATGTCTCCAACGTAAATCAAATAAA-3'	Cloning of truncated *ALG7* from *N*-terminus to LR4
AG7 (LR5)BPrv	5'-gcctttggccgaggcggccCAAATCAACACTAGTCTTTTTCAACC-3'	Cloning of truncated *ALG7* from *N*-terminus to LR5
AG7 (LR6)BPrv	5'-gcctttggccgaggcggccCCATTAACACCTGCCAGGATGTTG-3'	Cloning of truncated *ALG7* from *N*-terminus to LR6
AG7 (LR7)BPrv	5'-gcctttggccgaggcggccGAGTCTCTTGTGGCTAATGGCCC-3'	Cloning of truncated *ALG7* from *N*-terminus to LR7
AG7 (LR8)BPrv	5'-gcctttggccgaggcggccCCCACAAACACTGTGGCGGGC-3'	Cloning of truncated *ALG7* from *N*-terminus to LR8
AG7 (LR9)BPrv	5'-gcctttggccgaggcggcCTTTGAAAAATGACCCAGTATACCAA-3'	Cloning of truncated *ALG7* from *N*-terminus to LR9
AG7 (LR10)BPrv	5'-gcctttggccgaggcggccttGTATTGCACAATTTGTCTTCCCTCA-3'	Cloning of truncated *ALG7* from *N*-terminus to LR10

the pBT-N and pBT-STE vectors, respectively (Fig. 2).

2.3 *Assays for the membrane topology of Alg7p*

The bait constructs (the pBT-N-AG7, pBT-STE-AG7 and nine pBT-STE-hAG7/LR series) were used for co-transformation of yeast NMY51 strain, together with the negative control prey construct (pDL-Alg5) or positive control prey construct (pAI-Alg5). The transformation of the yeast cells was carried out by the standard method[30].

The co-transformants obtained on the synthetic dextrose (SD) medium lacking leucine and tryptophan (SD-LW) were then subject to the growth examination on the SD medium lacking leucine, tryptophan and histidine (SD-LWH) and SD medium lacking leucine, tryptophan, histidine and adenine (SD-LWHA) according to the manual supplied by Dualsystems Biotech (www.dualsystems.com).

2.4 *Assays for the physical interaction of Alg7p*

The bait construct, pBT-N-AG7 or pBT-STE-AG7, was combined with the prey construct, pPR-N-AG7 or pPR-STE-AG7, and then they were used for co-transformation of yeast NMY51 strain. After the co-transformation, the co-transformants grown on SD-LW medium were subject to growth examination with SD-LWH and SD-LWHA media, according to the same procedure as described above.

3. Results and Discussion

3.1 *The membrane topology of Alg7p*

The Alg7p protein is composed of 448 amino acid residues[3]. First, we started from predicting the membrane topology of Alg7p with TOPCONS algorithm[26], a freely

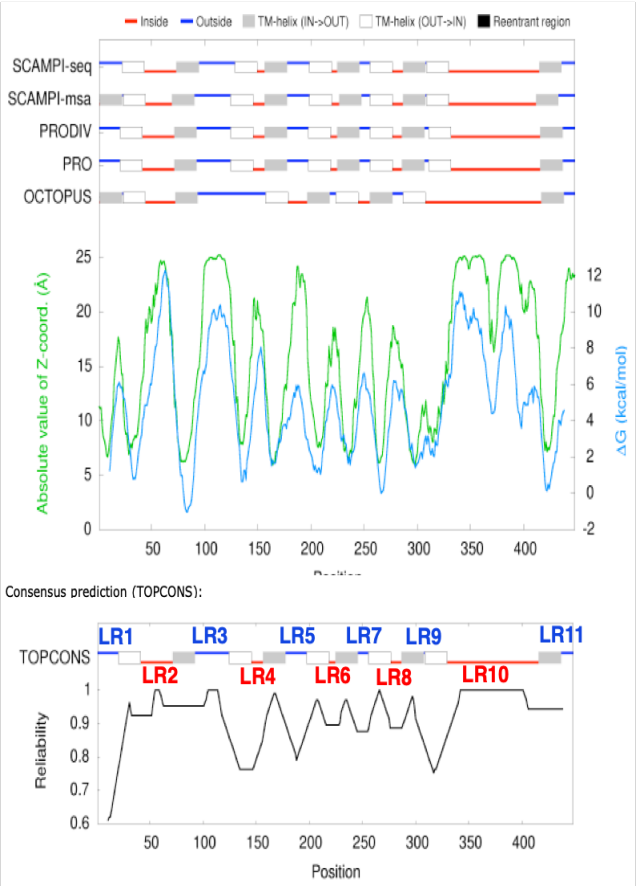

Fig. 1 Prediction of the membrane topology of Alg7p by TOPCONS algorithm server (http://topcons.cbr.su.se/). The ten hydrophobic regions (HR1 to HR10) are indicated with boxes, as candidates of transmembrane domains (TMDs), and the eleven loop regions (LR1 to LR11) are indicated with blue or red lines, as cytoplasmic or luminal loops, respectively.

available through WEB site. It consists of five independent algorithms (SCAMPI-seq, SCAMPI-msa, PRODIV, PRO and OCTOPUS in Fig. 1) that predict TMDs and membrane topology of a protein. Based on five predictions derived from their algorithms, TOPCONS concludes one consensus prediction. As shown in Fig. 1, TOPCONS consequently predicted eleven loop regions (LRs 1 to 11) and ten hydrophobic regions (HRs 1 to 10) corresponding to potential TMDs in Alg7p. It also predicted that both *N*- and *C*- termini would be orientated toward cytoplasmic sides of the rER membrane.

In order to examine this prediction, we applied the YSUS to our analysis of Alg7p. The YSUS prepares two prey constructs (pDL-Alg5 and pAI-Alg5) as negative and positive control, respectively. pAI-Alg5 is designed to express Nub I (*N*-terminal half of ubiquitin protein) tag *C*-terminally fused to Alg5p protein on the cytoplasmic side of the rER, and readily available to judge whether the terminal Cub tag fused to the bait protein expressed on the rER membrane is located in the cytoplasm or lumen[15-25]. Firstly, we prepared the two bait constructs, pBT-N-AG7 and pBT-STE-AG7, which express a full-length Alg7p protein with *N*- and *C*-terminal Cub tags, respectively (Fig. 2). Each bait construct was combined with the pDL-Alg5 or pAI-Alg5 control prey, and then they were used for co-transformation of yeast NMY51 cells. As shown in Fig. 3, co-transformants of pBT-N-AG7 or pBT-STE-AG7 with pDL-Alg5 did not grow on the two selective media (SD-LWH and SD-WWHA), but those with pAI-Alg5 grew on them (top and bottom red frames, respectively). These results indicated that both termini of Alg7p were located in the cytosol (Fig. 5). Next, we prepared nine additional bait constructs, pBT-STE-AG7/LR2 to pBT-STE-AG7/LR10, each of which would express truncated Alg7p protein, which has Cub tag at *C*-terminus (Fig. 2) and conducted similar growth examination. As a result, only co-transformants of pBT-STE-AG7/LR3, pBT-STE-AG7/LR4, pBT-STE-AG7/LR5, pBT-STE-AG7/LR6 or pBT-STE-AG7/LR7 with pAI-Alg5 displayed selective viability on two selective media (red frames in Fig. 3). These observations suggested that the LR3, LR4, LR5, LR6 and LR7 of Alg7p might be located in the cytoplasmic side of the rER membrane (Fig. 5). In contrast, co-transformants of pBT-STE-AG7/LR2, pBT-STE-AG7/LR8, pBT-STE-AG7/LR9 or pBT-STE-AG7/LR10 with pAI-Alg5 did not grow on two selective media (green frames in Fig. 3). These observations suggested that the LR2, LR8, LR9 and LR10 of Alg7p might be located in the luminal side of the rER membrane (Fig. 5).

Taken together, our membrane topological analysis of Alg7p demonstrated that it has at least four TMDs with *N*- and *C*- termini oriented towards cytosol, as a topological model proposed in Fig. 5. This model differs from that predicted in Fig. 2, with regard to the number of TMD. Although the possibility that the HR3, HR4, HR5, HR6, HR8 and HR9 of Alg7p would be potential membrane-embedded domains cannot be excluded, our model is so far the only one which were exhibited based on the experimental evidence.

Alg7p possesses a conserved DDxx motif, which might bind UDP-GlcNAc in the LR4 positioned between the HR 3 and HR4 (Fig. 5). Therefore, the LR4 must be located in the

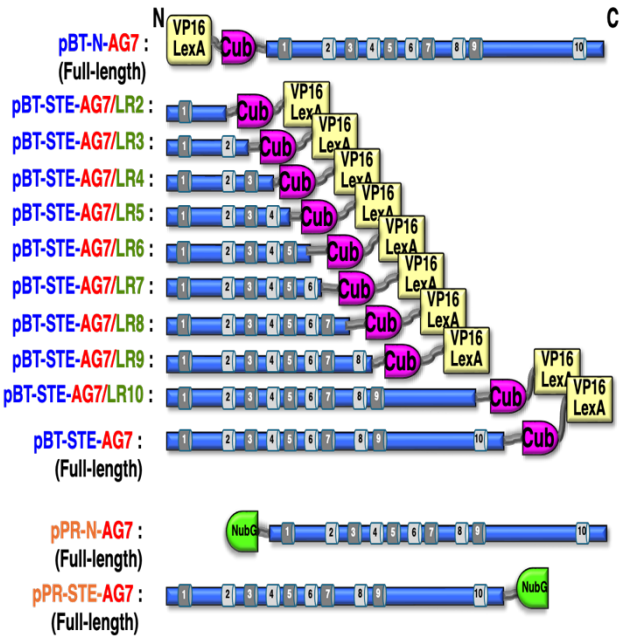

Fig. 2 Plasmid constructs and expressed proteins in this study. Bars and boxes of proteins indicate loop regions (LRs) and hydrophobic regions (HRs), respectively.

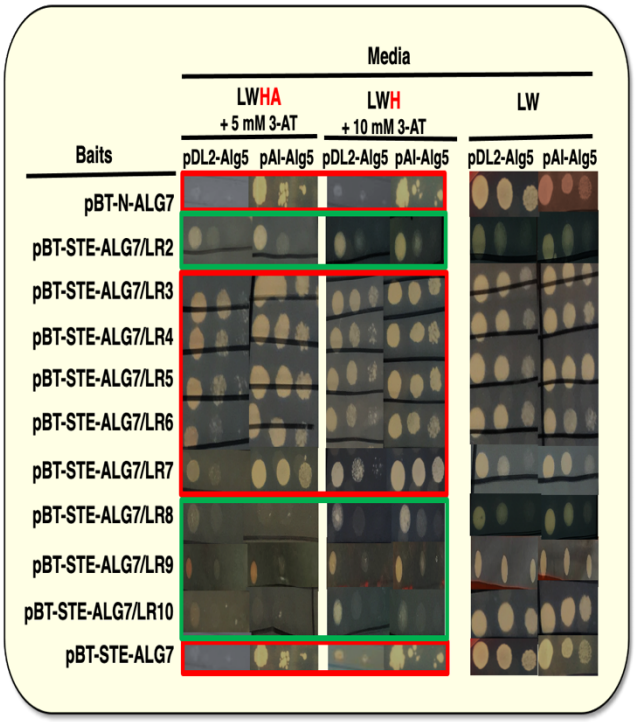

Fig. 3 Growth examination of co-transformants using two full-length Alg7p baits and nine truncated Alg7p baits. After the selection of colonies derived from the co-transformants on the SD-LW medium, their suspensions were diluted with sterilized water and adjusted to the OD_{600} values of 1.0, 0.1 and 0.01 (from left to right). These diluents were orderly spotted on the SD-LWH and SD-LWHA media for reporter detection, and SD-LW media for growth control, and then incubated at 30 ºC for 2~4 days. 3-amino-triazole (3-AT) was added to SD-LWH and SD-LWHA media at concentration of 10 and 5 mM respectively, for preventing background growth due to leaky *HIS3* gene expression.

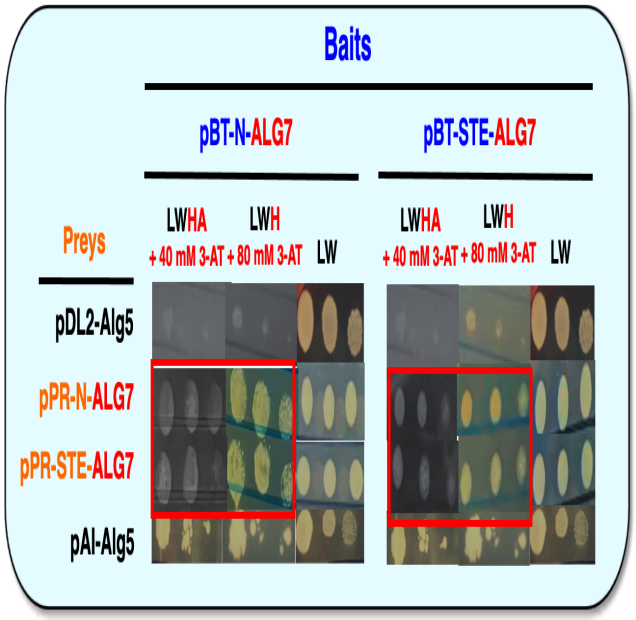

Fig. 4 Growth examination of co-transformants of pBT-N-AG7 or pBT-STE-AG7 with pPR-N-AG7 or pPR-STE-AG7. The experiments were carried out according to the same procedure as described in the legend of Fig. 3, except usage of LWH medium containing 80 mM 3-AT and LWHA medium containing 40 mM 3-AT.

cytoplasm, because UDP-GlcNAc is biosynthesized in the cytoplasm. Hence, our model is well suitable for this fact.

3.2 *The self-interaction of Alg7p*

In order to test whether Alg7p physically interacts with itself, each of the two bait constructs pBT-N-AG7 and pBT-STE-AG7, was combined with each of the two prey constructs, pPR-N-AG7 and pPR-STE-AG7, and then transformation of the NMY51 cells were conducted. In growth examination shown in Fig. 4, co-transformants of the four combinations could all grow on SD-LWH and SD-LWHA media (red frames in Fig. 4). This result suggests that Alg7p might tightly interact with itself.

.

4. Conclusion

In order to determine the membrane topology of yeast Alg7p which produces GlcNAc-PP-Dol, the YSUS was utilized. Results obtained from analyses by the YSUS demonstrated that Alg7p protein contains at least four TMDs, with both *N*- and *C*-termini located in the cytoplasmic side of the rER membrane (Fig. 3 and Fig. 5).

With respect to the physical interactions of Alg7p, we obtained a novel information strongly suggesting that it might homodimerize on the rER membrane (Fig. 4). It is possible to identify a region required for this self-interaction, by using a series of bait constructs for expression of truncated Alg7p baits, which we prepared in this study. In addition. we are now preparing a series of prey constructs for expression of truncated Alg7p preys to explore the interacting region.

The physical interaction between two membrane

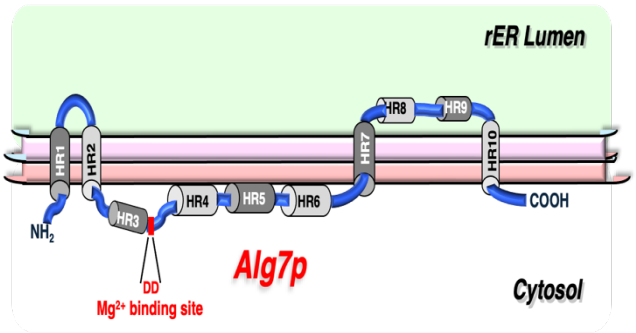

Fig. 5 The model of membrane topology of Alg7p based on the YSUS analyses indicated in Fig. 3. A conserved Mg^{2+} binding motif (DDxx) is indicated.

enzymes could play a role in positively or negatively altering their enzymatic activities. In this study, we found out that Alg7p forms at least homo-dimeric complex on the rER membrane. This fact raises the possibility that GPT activity might be regulated by the status of homo-oligomerization of Alg7p at protein level. On the other hand, we recently demonstrated that Alg5p bait physically interacts with Alg7p prey in another YSUS analysis[23]. This observation means that Alg7p might also form hetero-dimeric complex on the rER membrane. Hence, we are now investigating the physical interactions of Alg7p bait with preys of other enzymes involved in DLO assembly.

References

1) M. Aebi, *N*-linked protein glycosylation in the ER, Biochim. Biophys. Acta Vol.1833, pp.2430-2437 (2013).
2) J. Rine, W. Hansen, E. Hardeman and R. W. Davis, Targeted selection of recombinant clones through gene dosage effects, Proc. Natl. Acad. Sci. USA Vol.80, pp.6750-6754 (1983).
3) G. Barnes, W. J. Hansen, C. L. Holcomb and J. Rine, Asparagine-linked glycosylation in *Saccharomyces cerevisiae*: genetic analysis of an early step, Mol. Cell Biol. Vol.4, No.11, pp.2381-2388 (1984).
4) J. R. Scocca and S. S. Krag, Sequence of a cDNA that specifies the uridine diphosphate *N*-acetyl-D-glucosamine: dolichol phosphate *N*-acetylglucosamine-1-phosphate transferase from Chinese hamster ovary cells. J. Biol. Chem. Vol.265, pp.20621–26026 (1990).
5) B. Rajput, M. A. Jie, N. Muniappa, L. Schantz, S. L. Naylor, P. A. Lalley and I. K. Vijay, Mouse UDP-GlcNAc: dolichyl-phosphate *N*-acetyl- glucosamine-phosphotransferase: molecular cloning of the cDNA, generation of anti-peptide antibodies and chromosomal localization, Biochem. J. Vol.285, pp.985-992 (1992).
6) V. Eckert, M. Blank, R. Mazhari-Tabrizi, D. Mumberg, M. Funk and R. T. Schwarz, Cloning and functional expression of the human GlcNAc-1-P transferase, the enzyme for the committed step of the dolichol cycle, by heterologous complementation in *Saccharomyces cerevisiae*, Glycobiology Vol.8, pp.77–85 (1998).

7) N. Johnsson and A. Varshavsky, Split ubiquitin as a sensor of protein interactions *in vivo*, Proc. Natl. Acad. Sci. USA Vol.91, No.22, pp.10340-10344 (1994).
8) I. Stagljar, C. Korostensky, N. Johnsson and S. te Heesen, A genetic system based on split-ubiquitin for the analysis of interactions between membrane proteins *in vivo*, Proc. Natl. Acad. Sci. USA Vol.95, pp.5187-5192 (1998).
9) M. Fetchko and I. Stagljar, Application of the split-ubiquitin membrane yeast two-hybrid system to investigate membrane protein interactions, Methods Vol.32, pp.349-362 (2004).
10) S. Thaminy, J. Miller and I. Stagljar, The split-ubiquitin membrane-based yeast two-hybrid system, Methods. Mol. Biol. Vol.261, pp.297–312 (2004).
11) M. Dünnwald, A. Varshavsky and N. Johnsson, Detection of transient *in vivo* interaction between substrate and transporter during protein translocation into the endoplasmic reticulum, Mol. Biol. Cell Vol.10, pp.329-344 (1999).
12) M. J. Massaad and A. Herscovics, Interaction of the endoplasmic reticulum alpha 1, 2-mannosidase Mns1p with Rer1p using the split-ubiquitin system, J, Cell Sci. Vol.114, pp.4629-4635 (2001).
13) W. Scheper, S. Thaminy, S. Kais, I. Stagljar and K. Römisch, Coordination of *N*-glycosylation and protein translocation across the endoplasmic reticulum membrane by Sss1 protein, J. Biol. Chem. Vol.278, No.39, pp.37998-38003 (2003).
14) A. Yan and W. J. Lennarz, Studies on yeast oligosaccharyl transferase subunits using the split-ubiquitin system: Topological features and *in vivo* interactions, Proc. Natl. Acad. Sci. USA Vol.102, No.20, pp.7121-7126 (2005).
15) T. Takahashi and T. Takeuchi, Membrane topological characterization of the human Alg14 protein, Proc. Schl. Eng. Tokai Univ., Ser. E Vol.44, pp.1-6 (2019).
16) Samantha and T. Takahashi, Analyses of the membrane topology and physical interaction of dolichyl-phosphate-glucose synthase Alg5p, Proc. Schl. Eng. Tokai Univ., Ser. E Vol.49, pp.19-25 (2024).
17) T. Takahashi and X. -D. Gao, Physical interactions among human glycosyltransferases involved in dolichol-linked oligosaccharide biosynthesis, Trends in Glycoscience and Glycotechnology Vol.24, No.136, pp.65-77 (2012).
18) T. Takahashi, N. Yamada and N. Kurimoto, Analyses on the physical interactions of the human dolichyl-phosphate-mannose synthase, Proc. Schl. Eng. Tokai Univ., Ser. J. Vol.57, No.1, pp.5-10 (2017).
19) T. Takahashi, K. Nishimura, N. Maeda and R. Oshiro, Characterization of the membrane topology and physical interaction of human *N*-acetylglucosamine-1-phosphate transferase, Proc. Schl. Eng. Tokai Univ., Ser. E Vol.46, pp.1-6 (2021).
20) T. Takahashi, N. Yamada and R. Oshiro, Characterization of the membrane topology and physical interaction of human dolichol-phosphate-glucose synthase, Proc. Schl. Eng. Tokai Univ., Ser. E Vol.47, pp.1-6 (2022).
21) T. Takahashi, E. Horigome, T. Yamanoto and K. Terajima, Analyses of the membrane topology and physical interaction of human dolichol kinase, Proc. Schl. Eng. Tokai Univ., Ser. E Vol.49, pp.13-18 (2024).
22) K. Terajima, T. Yamamoto, C. Sugimura and T. Takahashi, Analyses of the physical interactions of human dolichol kinase with other dolichol-related enzymes involved in the dolichol cycle, Proc. Schl. Eng. Tokai Univ., Ser, E vol.50, pp.1-6 (2025).
23) Samantha, N. Adachi and T. Takahashi, Analyses of the physical interactions of yeast Alg5p with dolichyl-phosphate-related enzymes in the dolichol cycle, Proc. Schl. Eng. Tokai Univ., Ser, E Vol.50, pp.7-11 (2025).
24) T. Takahashi, T. Miyazaki and K. Sasaki, Characterization of the membrane topology of human chitobiosyldiphosphodolichol beta-1,4-mannosyltransferase, Proc. Schl. Eng. Tokai Univ., Ser, E Vol.50, pp.13-17 (2025).
25) T. Takahashi, K. Kurihara and Y. Shiraiwa, Characterization of the membrane topology and self-interaction of yeast dolichol kinase Sec59p, Proc. Schl. Eng. Tokai Univ., Ser, E Vol.50, pp.19-23 (2025).
26) K. D. Tsirigos, C. Peters, N. Shu, L. Käll and A. Elofsson, The TOPCONS web server for consensus prediction of membrane protein topology and signal peptides, Nucleic Acids Res. 43(Web Server issue) W401-407 (2005).
27) H. A. Erlich, PCR Technology, Stockton Press, pp.61-70 (1989).
28) H. Inoue, H. Nojima and H. Okayama, High efficiency transformation of *Escherichia coli* with plasmids, Gene Vol. 96, pp.23–28 (1990).
29) L. Sambrook, E. F. Fritsch and T. Maniatis, Molecular Cloning: A Laboratory Manual. Second edition, Cold Spring Harbor Laboratory Press, NY, (1989).
30) H. Ito, Y. Fukuda, K. Murata and A. Kimura, Transformation of intact yeast cells treated with alkali cations, J. Bacteriol. Vol.153, No.1, pp.163-168 (1983).

Proc. Schl. Eng. Tokai Univ., Ser. E
51 (2026) 7-12
DOI: 10.18995/24343641. 51. 7

Characterization of the Membrane Topology and Physical Interaction of Yeast Cwh8p

by

Tetsuo TAKAHASHI*1, Maria TERAI*2 and Kurumi YAMAMOTO*2

(Received on Apr. 8, 2026 and accepted on May 25, 2026)

Abstract

Cwh8p is a yeast dolichyl pyrophosphatase, which produces dolichyl phosphate (Dol-P) from dolichyl pyrophosphate (Dol-PP). Produced Dol-P is required for *N*-acetylglucosamine-1-phosphate (GlcNAc-1-P) transferase, dolichyl phosphate mannose (Dol-P-Man) synthase and dolichyl phosphate glucose (Dol-P-Glc) synthase in the biosynthetic pathway of dolichol-linked oligosaccharide (DLO). Here we used the yeast *CWH8* gene to analyze the membrane topology and physical interaction of Cwh8p by the yeast split-ubiquitin system (YSUS). Our research revealed that Cwh8p has at least four transmembrane domains (TMDs) with both termini oriented toward the cytoplasmic side of the rough ER (rER) membrane. In addition, it was revealed that Cwh8p physically interacts with itself and yeast dolichol kinase Sec59p, suggesting that it might function in the forms of both homodimer and heterodimer.

***Keywords*:** Dolichyl pyrophosphatase, Membrane topology, Physical interaction, Split-ubiquitin system

1. Introduction

Protein *N*-glycosylation is an essential event for viability of eukaryotes[1]. After the assembly of dolichol-linked oligosaccharide (DLO), oligosaccharyl transferase complex transfers an oligosaccharide portion from DLO into nascent protein to yield *N*-glycosylated protein and dolichyl pyrophosphate (Dol-PP) within the rough endoplasmic reticulum (rER). For sustainable production of DLO, enough amount of dolichyl phosphate (Dol-P) is always required. In budding yeast, Dol-P is *de novo* biosynthesized by dolichol kinase Sec59p[2]. In addition, yeast dolichyl pyrophosphatase Cwh8p[3] plays a central role in recycling of Dol-P from Dol-PP. In the assembly of DLO on the rER membrane, Dol-P is utilized by Alg7p[4], Dpm1p[5] and Alg5p[6], which are the *N*-acetylglucosamine-1-phosphate (GlcNAc-1-P) transferase (GPT), dolichyl phosphate mannose (Dol-P-Man) synthase (DPMS) and dolichyl phosphate glucose (Dol-P-Glc) synthase (DPGS), respectively.

We have been investigating the membrane topology and physical interaction of enzymes involved in DLO assembly by utilizing the yeast split-ubiquitin system (YSUS)[7-10], which has so far identified the physical interaction of various membrane proteins with other membrane proteins[11-26]. Recently, we have been successful in characterization of the membrane topology and physical interaction of human dolichyl pyrophosphatase (hDPP). Therefore, we tried to proceed the investigation for yeast Cwh8p using the YSUS.

*1 Associate Professor, Department of Bioengineering
*2 Undergraduate Student, Department of Bioengineering

2. Experimental Methods

2.1 *Prediction of the membrane topology of Cwh8p*

Firstly, we predicted the membrane topology of Cwh8p using a TOPCONS WWW algorithm server[26], (https://topcons. cbr.su.se). On its WEB site, the amino acid sequence of Cwh8p consisting of 239 residues was registered and surveyed about its potential transmembrane domains (TMDs) and membrane topology.

2.2 *Construction of recombinant plasmids for the YSUS*

The coding region of *CWH8* gene was amplified from genomic DNA derived from *Saccharomyces cerevisiae* NMY51 strain by standard PCR method[27] using CH8BPfw and CH8BPrv primers listed in Table 1. A PCR product was then digested with *Sfi* I, purified and ligated to the pBT-N or pBT-C plasmid vector for expression of Cwh8p bait protein which has Cub (*C*-terminal half of ubiquitin protein) tag prepared in the YSUS, at the *N*- or *C*- terminus, respectively. Subsequently, the ligation mix was used for transformation of *Escherichia coli* JM109 strain prepared by SEM method[28]. Preparation of each recombinant plasmid from the transformants was conducted by standard cloning method[29], generating pBT-N-CWH8 and pBT-C-CWH8 bait constructs (Fig. 2).

In order to analyze membrane topology of Cwh8p, four pBT-C-based constructs (pBT-C-CWH8/LR2 to pBT-C-CWH8/LR5) for expression of the *C*-terminally truncated Cwh8p bait

Table I The PCR primers used in this study. Additional sequences containing a *Sfi* I- cleavage site are shown in lowercase letters.

Primer name	Nucleotide sequence	Purpose
CH8BPfw	5'-tgtaatggccattacggccATGAATAGTACCGCCGCTGCAATAAAT-3'	Cloning of full-length and *C*-terminally truncated *CHW8*
CH8BPrv	5'-gcctttggccgaggcggccttATCCCTTTTGGATTTATCATTGAAAGATC-3'	Cloning of full-length and *N*-terminally truncated *CHW8*
CH8 (LR2)BPrv	5'-gcctttggccgaggcggccttGATGATAAACCACGACAAATAAAAAGC-3'	Cloning of truncated *CHW8* from *N*-terminus to LR2
CH8 (LR3)BPrv	5'-gcctttggccgaggcggcCCCGTAACCGGATCTTATAGTGTCATTTTGG -3'	Cloning of truncated *CHW8* from *N*-terminus to LR3
CH8 (LR4)BPrv	5'-gcctttggccgaggcggccTTTTCTAAGAAGTTTAGATTCTTCCAGG-3'	Cloning of truncated *CHW8* from *N*-terminus to LR4
CH8 (LR5)BPrv	5'-gcctttggccgaggcggccTGATCTAAATTGTGGTAGTGCAAGTAAACTC-3'	Cloning of truncated *CHW8* from *N*-terminus to LR5
CH8(*ΔN29*)BPfw	5'-tgtaatggccattacggccatgCTATCATTCCTTAGTGCATATTTCTCG-3'	Cloning of *N*-terminally truncated *CHW8*

proteins in yeast were prepared via PCR cloning described above (Fig. 2).

For analysis of the self-interaction of Cwh8p, the prey constructs (pPR-N-CWH8 and pPR-C-CWH8) that would express Cwh8p prey protein having Nub G (*N*-terminal half of I13G mutational ubiquitin protein) tag at the *N*- or *C*-terminus, were prepared by the same procedure, except usage of the pPR-N and pPR-C plasmid vectors instead of the pBT-N and pBT-C vectors, respectively (Fig. 2). Moreover, two additional prey constructs (pPR-N-CWH8/LR2 and pPR-N-CWH8/*ΔN29*) for expression of the *N*- and *C*-terminally truncated Cwh8p bait proteins in yeast were also prepared via PCR cloning described above (Fig. 2).

For analysis of the physical interaction of Cwh8p with Sec59p, two prey constructs (pPR-N-SEC59 and pPR-C-SEC59)[25] that would express Sec59p prey protein having Nub G tag at the *N*- or *C*- terminus, were prepared.

2.3 *Assays for the membrane topology of Cwh9p*

The bait constructs (the pBT-N-CWH8, pBT-C-CWH8 and six pBT-C-CWH8/LR series) were used for co-transformation of yeast NMY51 strain, together with the negative control prey construct (pDL-Alg5) or positive control prey construct (pAI-Alg5). The transformation of the yeast cells was carried out by the standard method[30].

The co-transformants obtained on the synthetic dextrose (SD) medium lacking leucine and tryptophan (SD-LW) were then subject to the growth examination on the SD medium lacking leucine, tryptophan and histidine (SD-LWH) and SD medium lacking leucine, tryptophan, histidine and adenine (SD-LWHA) according to the manual supplied by Dualsystems Biotech (www.dualsystems.com).

2.4 *Assays for the physical interaction of Cwh8p*

The bait construct, pBT-N-CWH8 or pBT-C-CWH8, was combined with the prey construct, pPR-N-CWH8 or pPR-C-CWH8, and then they were used for co-transformation of yeast NMY51 strain. After the co-transformation, the co-transformants grown on SD-LW medium were subject to growth examination with SD-LWH and SD-LWHA media, according to the same procedure as described above.

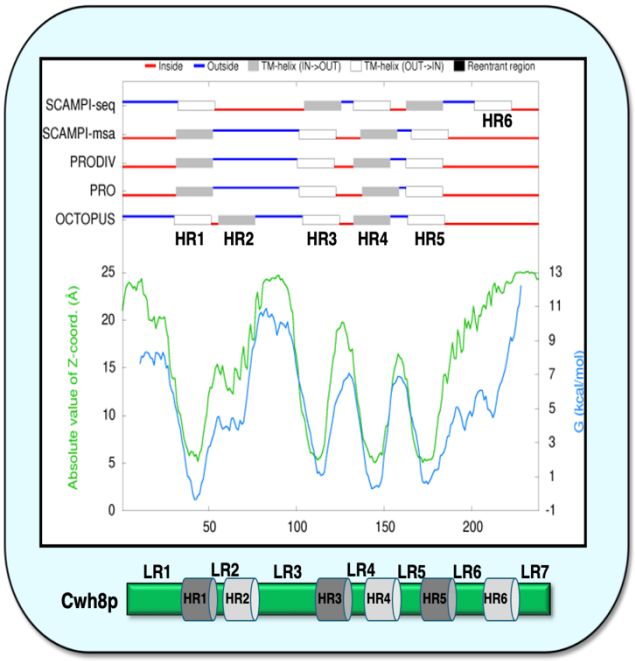

Fig. 1 Prediction of the membrane topology of Cwh8p by TOPCONS algorithm server (http://topcons.cbr.su.se/). The six hydrophobic regions (HR1 to HR6) are indicated with boxes, as candidates of transmembrane domains (TMDs), and the seven loop regions (LR1 to LR7) are indicated with bars, as cytoplasmic or luminal loops.

3. Results and Discussion

3.1 *The membrane topology of Cwh8p*

The Cwh8p protein is composed of 239 amino acid residues[3]. First, we started from predicting the membrane topology of Cwh8p with TOPCONS algorithm[26], a server freely available on WEB sites. It consists of five independent algorithms (SCAMPI-seq, SCAMPI-msa, PRODIV, PRO and OCTOPUS in Fig. 1) that predict TMDs and membrane topology of a protein. Based on five predictions derived from their algorithms, TOPCONS concludes one consensus prediction. As shown in Fig. 1, TOPCONS conclusively predicted seven loop regions (LRs 1 to 7) and six hydrophobic regions (HRs 1 to 6) corresponding to potential

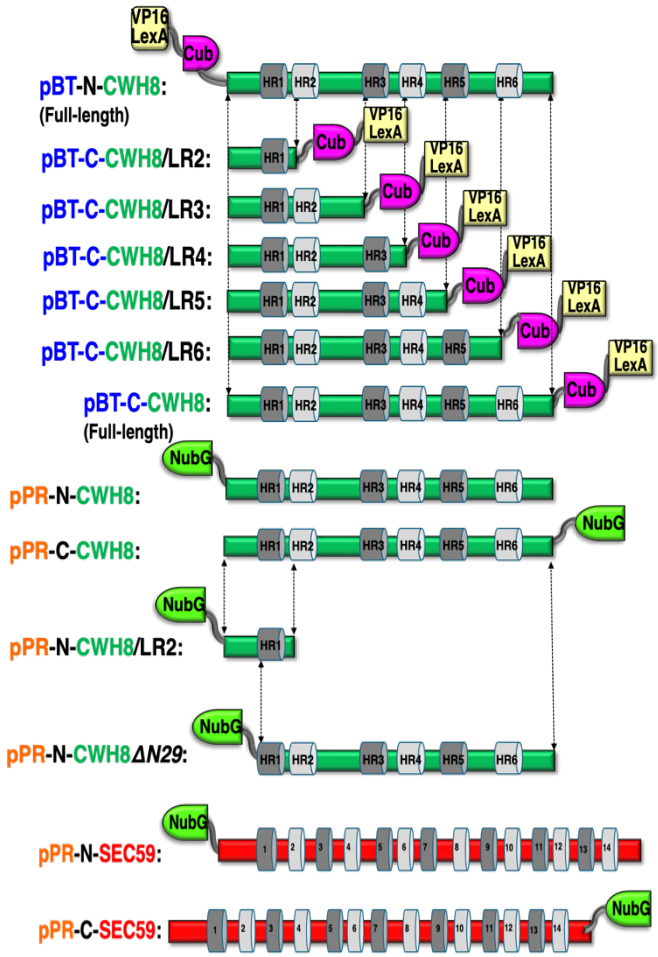

Fig. 2 Plasmid constructs and expressed proteins in this study. Cub-VP16/LexA and Nub G tags are fused to *N*- or *C*-terminus of the proteins for the YSUS analysis. Bars and boxes of proteins indicate loop regions (LRs) and hydrophobic regions (HRs), respectively.

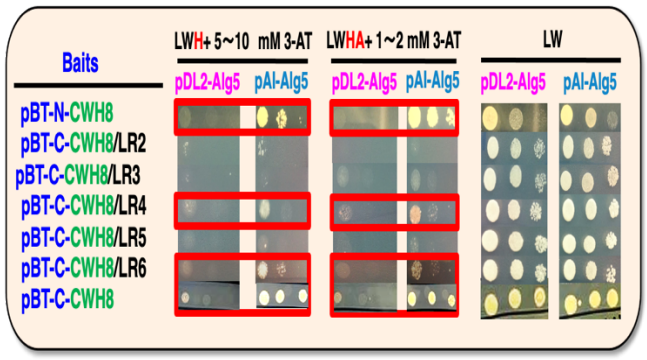

Fig. 3 Growth examination of co-transformants using two full-length Cwh8p baits and five truncated Cwh8p baits. After the selection of colonies derived from the co-transformants on the SD-LW medium, their suspensions were diluted with sterilized water and adjusted to the OD_{600} values of 1.0, 0.1 and 0.01 (from left to right). These diluents were orderly spotted on the SD-LWH and SD-LWHA media for reporter detection, and SD-LW media for growth control, and then incubated at 30 ºC for 2~4 days. 3-amino-triazole (3-AT) was added to SD-LWH and SD-LWHA media at concentration of 5-10 and 1-2 mM respectively, for preventing background growth due to leaky *HIS3* gene expression.

TMDs in Cwh8p. It also predicted that both *N*- and *C*- termini would be orientated toward cytoplasmic sides of the rER membrane.

In order to examine this prediction, we applied the YSUS to our analysis of Cwh8p. The YSUS prepares two prey constructs (pDL-Alg5 and pAI-Alg5) as negative and positive control, respectively. pAI-Alg5 is designed to express Nub I (*N*-terminal half of ubiquitin protein) tag *C*-terminally fused to Alg5p protein on the cytoplasmic side of the rER, and readily available to judge whether the terminal Cub tag fused to the bait protein expressed on the rER membrane is located in the cytoplasm or lumen[15-25]. Firstly, we prepared the two bait constructs, pBT-N-CWH8 and pBT-C-CWH8, which express a full-length Cwh8p protein with *N*- and *C*-terminal Cub tags, respectively (Fig. 2). Each bait construct was combined with the pDL-Alg5 or pAI-Alg5 control prey, and then they were used for co-transformation of yeast NMY51 cells. As shown in Fig. 3, co-transformants of pBT-N-CWH8 or pBT-C-CWH8 with pDL-Alg5 did not grow on the two selective media (SD-LWH and SD-WWHA), but those with pAI-Alg5 grew on them (top and bottom red frames, respectively). These results indicated that both termini of Cwh8p were located in the cytosol (Fig. 5).

Next, we prepared five additional bait constructs, pBT-C-CWH8/LR2 to pBT-C-CWH8/LR6, each of which would express truncated Cwh8p protein, which has Cub tag at *C*-terminus (Fig. 2) and conducted similar growth examination. As a result, only co-transformants of pBT-C-CWH8/LR4 or pBT-C-CWH8/LR6 with pAI-Alg5 displayed selective viability on two selective media (red frames in Fig. 3). These observations suggested that the LR4 and LR6 of Cwh8p might be located on the cytoplasmic side of the rER membrane (Fig. 5). In contrast, co-transformants of pBT-C-CWH8/LR2, pBT-C-CWH8/LR3 or pBT-C-CWH8/LR5 with pAI-Alg5 did not grow on two selective media (Fig. 3). These observations suggested that the LR2, LR3 and LR5 of Cwh8p might be located on the luminal side of the rER membrane (Fig. 5).

Taken together, our membrane topological analysis of Cwh8p demonstrated that it has at least four TMDs with *N*- and *C*- termini oriented towards cytosol, as a topological model proposed in Fig. 5. This model differs from that predicted in Fig. 2, with regard to the number of TMD. Although the possibility that the HR2 and/or HR6 of Cwh8p would be potential membrane-embedded domains cannot be excluded, our model is so far the only one which were exhibited based on the experimental evidence.

Cwh8p possesses a conserved lipid phosphate phosphatase motif around the LR3 and LR5 (Fig. 5). Therefore, these two loops must be located within the rER lumen, because dephosphorylation of Dol-PP indeed occurs on the luminal side of the rER membrane. Hence, our model is well suitable for this fact.

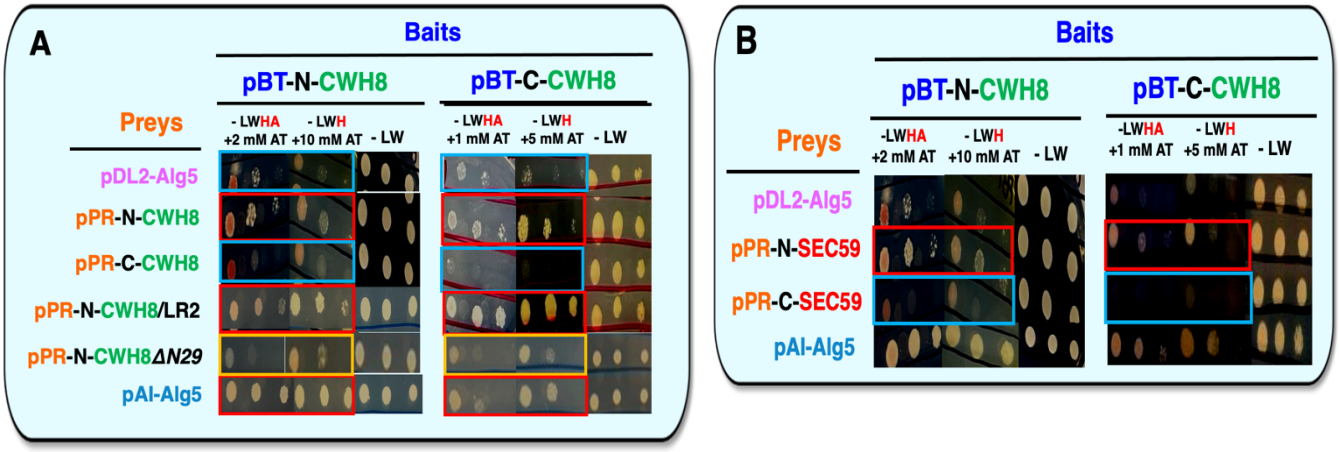

Fig. 4 (A) Growth examination of co-transformants of pBT-N-CWH8 or pBT-C-CWH8 with pPR-N-CWH8, pPR-C-CWH8, pPR-N-CWH8/LR2 or pPR-N-CWH8/*ΔN29*. (B) Growth examination of co-transformants of pBT-N-CWH8 or pBT-C-CWH8 with pPR-N-SEC59 or pPR-C-SEC59. Each experiment was carried out according to the same procedure as described in the legend of Fig. 3.

3.2 *The physical interaction of Cwh8p*

In order to test whether Cwh8p physically interacts with itself, each of the two bait constructs pBT-N-CWH8 and pBT-C-CWH8, was combined with each of the two prey constructs, pPR-N-CWH8 and pPR-C-CWH8, and then transformation of the NMY51 cells was conducted. In growth examination shown in Fig. 4A, co-transformants of pBT-N-CWH8 or pBT-C-CWH8 with pPR-N-CWH8 could grow on SD-LWH and SD-LWHA media (red frames), but those with pPR-C-CWH8 could not (blue frames). These results indicate that both termini of Cwh8p bait would be sufficiently proximal to *N*-terminus, but distal to *C*-terminus of Cwh8p prey, probably due to conformational reason. By taking advantage of this proximity between two *N*-termini of Cwh8p bait and prey, we further explored a region critical for self-interaction of Cwh8p. Co-transformants of pBT-N-CWH8 or pBT-C-CWH8 with pPR-N-CWH8/LR2 could normally grow on SD-LWH and SD-LWHA media, but those with pPR-N-CWH8/*ΔN29* greatly reduced cellular viability (orange frames in Fig 4A). These observations strongly suggested that the *N*-terminal LR1 of Cwh8p might be associated with self-interaction of Cwh8p.

In order to test whether Cwh8p physically interacts with dolichol kinase Sec59p, each of the two bait constructs pBT-N-CWH8 and pBT-C-CWH8, was combined with each of the two prey constructs, pPR-N-SEC59 and pPR-C-SEC59. In growth examination shown in Fig. 4B, co-transformants of pBT-N-CWH8 or pBT-C-CWH8 with pPR-N-SEC59 could grow on SD-LWH and SD-LWHA media (red frames), indicating that Cwh8p is also able to physically interact with Sec59p. However, co-transformants of pBT-N-CWH8 or pBT-C-CWH8 with pPR-C-SEC59 could not grow (blue frames). These results indicate that *N*-terminus of Sec59p prey would be sufficiently proximal to both termini of Cwh8p bait, but *C*-terminus of the prey Cwh8p would not.

4. Conclusion

In order to determine the membrane topology of yeast Cwh8p which reproduces Dol-P, the YSUS was utilized. Results obtained from analyses by the YSUS demonstrated that Cwh8p protein contains at least four TMDs, with both *N*- and *C*-termini located on the cytoplasmic side of the rER membrane (Fig. 3 and Fig. 5).

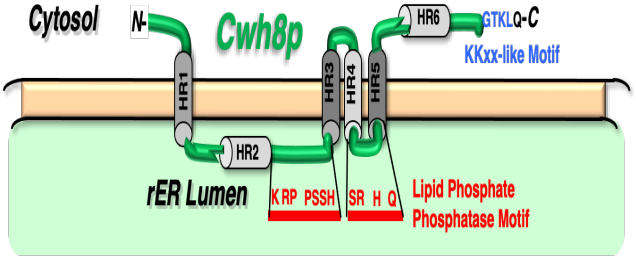

Fig. 5 The model of membrane topology of Cwh8p based on the YSUS analyses indicated in Fig. 3. The conserved lipid phosphate phosphatase motif is indicated in red color.

With respect to the physical interactions of Cwh8p, we obtained a novel information strongly suggesting that it might homodimerize with Cwh8p or heterodimerize with Sec59p on the rER membrane (Fig. 4). It is possible to refine a region required for these interactions, by using a series of constructs for expression of truncated Cwh8p bait or prey, which we prepared in this study. Now we are preparing a series of prey constructs for expression of truncated Cwh8p preys to explore the interacting region.

The physical interaction between two membrane enzymes could play a role in positively or negatively altering their enzymatic activities. In this study, we found out that Cwh8p forms homo- or hetero- dimeric complex on the rER membrane. This fact raises the possibility that Dol-PP phosphatase activity might be regulated by the status of oligomerization of Cwh8p at protein level. To prove this possibility, biochemical and stoichiometry analyses of Cwh8p will be further required. On the other hand, we recently demonstrated that Alg5p bait physically interacts with Cwh8p prey in another YSUS analysis[23]. This

observation means that Cwh8p might also form other hetero-dimeric complex on the rER membrane. Hence, we are now investigating the physical interactions of Cwh8p bait with preys of other enzymes involved in DLO assembly.

References

1) M. Aebi, *N*-linked protein glycosylation in the ER, Biochim. Biophys. Acta Vol.1833, pp.2430-2437 (2013).
2) L. Heller, P. Orlean and W. L. Adair Jr., *Saccharomyces cerevisiae* sec59 cells are deficient in dolichol kinase activity, Proc. Natl. Acad. Sci. USA Vol.89, pp.7013-7016 (1999).
3) M. A. van Berkel, M. Rieger, S. te Heesen, A. F. Ram, H. van den Ende, M. Aebi and F. M. Klis, The *Saccharomyces cerevisiae CWH8* gene is required for full levels of dolichol-linked oligosaccharides in the endoplasmic reticulum and for efficient *N*-glycosylation, Glycobiology Vol.9, No.3, pp.243–253 (1990).
4) G. Barnes, W. J. Hansen, C. L. Holcomb and J. Rine, Asparagine-linked glycosylation in *Saccharomyces cerevisiae*: genetic analysis of an early step, Mol. Cell Biol. Vol.4, No.11, pp.2381-2388 (1984).
5) P. Orlean, Dolichol phosphate mannose synthase is required *in vivo* for glycosyl phosphatidylinositol membrane, Mol. Cell Biol. Vol.10, No.11, pp.5796-5805 (1990).
6) S. te Heesen, L. Lehle, A. Weissmann and M. Aebi, Isolation of the *ALG5* locus encoding the UDP-glucose: dolichyl-phosphate glucosyltransferase from S*accharomyces cerevisiae*. Eur. J. Biochem. Vol.224, pp.71-79 (1994).
7) N. Johnsson and A. Varshavsky, Split ubiquitin as a sensor of protein interactions *in vivo*, Proc. Natl. Acad. Sci. USA Vol.91, No.22, pp.10340-10344 (1994).
8) I. Stagljar, C. Korostensky, N. Johnsson and S. te Heesen, A genetic system based on split-ubiquitin for the analysis of interactions between membrane proteins *in vivo*, Proc. Natl. Acad. Sci. USA Vol.95, pp.5187-5192 (1998).
9) M. Fetchko and I. Stagljar, Application of the split-ubiquitin membrane yeast two-hybrid system to investigate membrane protein interactions, Methods Vol.32, pp.349-362 (2004).
10) S. Thaminy, J. Miller and I. Stagljar, The split-ubiquitin membrane-based yeast two-hybrid system, Methods. Mol. Biol. Vol.261, pp.297–312 (2004).
11) M. Dünnwald, A. Varshavsky and N. Johnsson, Detection of transient *in vivo* interaction between substrate and transporter during protein translocation into the endoplasmic reticulum, Mol. Biol. Cell Vol.10, pp.329-344 (1999).
12) M. J. Massaad and A. Herscovics, Interaction of the endoplasmic reticulum alpha 1, 2-mannosidase Mns1p with Rer1p using the split-ubiquitin system, J, Cell Sci. Vol.114, pp.4629-4635 (2001).
13) W. Scheper, S. Thaminy, S. Kais, I. Stagljar and K. Römisch, Coordination of *N*-glycosylation and protein translocation across the endoplasmic reticulum membrane by Sss1 protein, J. Biol. Chem. Vol.278, No.39, pp.37998-38003 (2003).
14) A. Yan and W. J. Lennarz, Studies on yeast oligosaccharyl transferase subunits using the split-ubiquitin system: Topological features and *in vivo* interactions, Proc. Natl. Acad. Sci. USA Vol.102, No.20, pp.7121-7126 (2005).
15) T. Takahashi and T. Takeuchi, Membrane topological characterization of the human Alg14 protein, Proc. Schl. Eng. Tokai Univ., Ser. E Vol.44, pp.1-6 (2019).
16) Samantha and T. Takahashi, Analyses of the membrane topology and physical interaction of dolichyl-phosphate-glucose synthase Alg5p, Proc. Schl. Eng. Tokai Univ., Ser. E Vol.49, pp.19-25 (2024).
17) T. Takahashi and X. -D. Gao, Physical interactions among human glycosyltransferases involved in dolichol-linked oligosaccharide biosynthesis, Trends in Glycoscience and Glycotechnology Vol.24, No.136, pp.65-77 (2012).
18) T. Takahashi, N. Yamada and N. Kurimoto, Analyses on the physical interactions of the human dolichyl-phosphate-mannose synthase, Proc. Schl. Eng. Tokai Univ., Ser. J. Vol.57, No.1, pp.5-10 (2017).
19) T. Takahashi, K. Nishimura, N. Maeda and R. Oshiro, Characterization of the membrane topology and physical interaction of human *N*-acetylglucosamine-1-phosphate transferase, Proc. Schl. Eng. Tokai Univ., Ser. E Vol.46, pp.1-6 (2021).
20) T. Takahashi, N. Yamada and R. Oshiro, Characterization of the membrane topology and physical interaction of human dolichol-phosphate-glucose synthase, Proc. Schl. Eng. Tokai Univ., Ser. E Vol.47, pp.1-6 (2022).
21) T. Takahashi, E. Horigome, T. Yamanoto and K. Terajima, Analyses of the membrane topology and physical interaction of human dolichol kinase, Proc. Schl. Eng. Tokai Univ., Ser. E Vol.49, pp.13-18 (2024).
22) K. Terajima, T. Yamamoto, C. Sugimura and T. Takahashi, Analyses of the physical interactions of human dolichol kinase with other dolichol-related enzymes involved in the dolichol cycle, Proc. Schl. Eng. Tokai Univ., Ser, E vol.50, pp.1-6 (2025).
23) Samantha, N. Adachi and T. Takahashi, Analyses of the physical interactions of yeast Alg5p with dolichyl-phosphate-related enzymes in the dolichol cycle, Proc. Schl. Eng. Tokai Univ., Ser, E Vol.50, pp.7-11 (2025).
24) T. Takahashi, T. Miyazaki and K. Sasaki, Characterization of the membrane topology of human chitobiosyl-diphospatedolichol beta-1,4-mannosyltransferase, Proc. Schl. Eng. Tokai Univ., Ser, E Vol.50, pp.13-17 (2025).
25) T. Takahashi, K. Kurihara and Y. Shiraiwa, Characterization of the membrane topology and self-interaction of yeast dolichol kinase Sec59p, Proc. Schl. Eng. Tokai Univ., Ser, E Vol.50, pp.19-23 (2025).
26) K. D. Tsirigos, C. Peters, N. Shu, L. Käll and A. Elofsson, The TOPCONS web server for consensus prediction of membrane protein topology and signal peptides, Nucleic Acids Res. 43(Web Server issue) W401-407 (2005).

27) H. A. Erlich, PCR Technology, Stockton Press, pp.61-70 (1989).
28) H. Inoue, H. Nojima and H. Okayama, High efficiency transformation of *Escherichia coli* with plasmids, Gene Vol. 96, pp.23–28 (1990).
29) L. Sambrook, E. F. Fritsch and T. Maniatis, Molecular Cloning: A Laboratory Manual. Second edition, Cold Spring Harbor Laboratory Press, NY, (1989).
30) H. Ito, Y. Fukuda, K. Murata and A. Kimura, Transformation of intact yeast cells treated with alkali cations, J. Bacteriol. Vol.153, No.1, pp.163-168 (1983).

Proc. Schl. Eng. Tokai Univ., Ser. E
51 (2026) 13-18
DOI: 10.18995/24343641. 51. 13

Identification of the Physical Interactions Between Dolichol-Related Enzymes and Mannosyltransferases Involved in the Early Assembly of Dolichol-Linked Oligosaccharide

by

Hanaka KOBORI[*1], Minami TANIMURA[*1], Aika KAWANO[*1] and Tetsuo TAKAHASHI[*2]

(Received on Apr. 10, 2026 and accepted on May 25, 2026)

Abstract

In yeast cells, three mannosyltransferases—Alg1p, Alg2p and Alg11p—are involved in the early assembly of dolichol-linked oligosaccharide (DLO). On the other hand, dolichyl phosphate (Dol-P), which is required for early DLO assembly is supplied by two dolichol-related enzymes: the dolichol kinase Sec59p and the dolichyl pyrophosphatase Cwh8p. In this study, we used the five yeast genes *ALG1*, *ALG2*, *ALG11*, *SEC59* and *CWH8* to analyze the physical interaction of the mannosyltransferases with dolichol-related enzymes by the yeast split-ubiquitin system (YSUS). Our results revealed that all three mannosyltransferases physically interact with both Sec59p and Cwh8p, suggesting that glycosyltransferases and dolichol-related enzymes might be closely collaborating in early DLO assembly.

Keywords: Dolichol-related enzyme, Mannosyltransferase, Physical interaction, Split-ubiquitin system

1. Introduction

In eukaryotic cells, dolichol localized on the rough endoplasmic reticulum (rER) membrane functions as a carrier for biosynthesis of various glycans, including *N*-glycans, glycosyl-phosphatidyl inositol (GPI) anchors and *C*-glycans. Among these, the dolichol-linked oligosaccharide (DLO), a precursor of *N*-glycan, has the most complex structure consisting of two *N*-acetylglucosamine (GlcNAc), nine mannose (Man) and three glucose (Glc) residues[1)]. In addition, as protein *N*-glycosylation is an essential event for cellular viability of eukaryotes, dolichol is considered as a key molecule for glycosylation. During the early stage of DLO assembly, a half-sized intermediate $Man_5GlcNAc_2$-PP-dolichol is formed on the cytoplasmic side of the rER membrane by seven glycosyltransferase activities (Fig. 1). In *Saccharomyces cerevisiae*, three mannosyltransferases (Alg1p, Alg2p and Alg11p), which utilize GDP-Man as a donor, are involved in this process. Alg1p[2)] is a β-1,4-mannosyltransferase (MT-I) that catalyzes the addition of the first Man residue to DLO. Alg2p[3)] possesses dual enzymatic activities, functioning first as an α-1,3-mannosyl transferase (MT-II) and subsequently as an α-1,6-mannosyl transferase (MT-III). Alg11p[4)] (MT-IV/V) catalyzes the addition of the fourth and fifth Man residues via α-1,2 linkage.

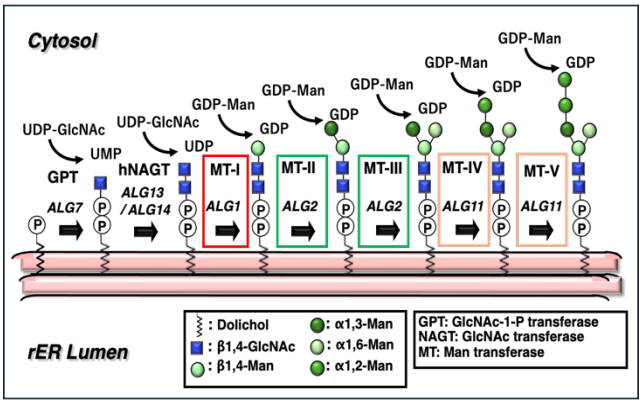

Fig. 1 Early stage of dolichol-linked oligosaccharide (DLO) biosynthesis in budding yeast. The upper names and lower italic names above arrows mean enzymes and yeast genes, respectively.

On the other hand, the production of dolichol phosphate (Dol-P) is essential for the utilization of dolichol in DLO assembly. Dol-P is generated through the phosphorylation of dolichol, catalyzed by the dolichol kinase Sec59p[5)], and through the dephosphorylation of dolichol pyrophosphate (Dol-PP), which is derived from DLO by the dolichol pyrophosphatase Cwh8p[6)].

The yeast split-ubiquitin system (YSUS) is a powerful technique that enables the detection of the physical interactions between two membrane proteins[7-10)]. Indeed, the physical interactions among various membrane proteins were indeed identified using this system[11-14)]. We have also been

*1 Undergraduate Student, Department of Bioengineering
*2 Associate Professor, Department of Bioengineering

Table I The PCR primers used in this study. Additional sequences containing a *Sfi* I- cleavage site are shown in lowercase letters.

Primer name	Nucleotide sequence	Cloning gene
AG1BPfw	5'-tgtaatggccattacggccATGTTTTTGGAAATTCCTCGGTGG-3'	Full-length *ALG1*
AG1BPrv	5'-gcctttggccgaggcggccCAATGAATTAGCTTCAAATCTCTC-3'	Full-length *ALG1*
AG2BPfw	5'-tgtaatggccattacggccATGATTGAAAAGGATAAAAGAACG-3'	Full-length *ALG2*
AG2BPrv	5'-gcctttggccgaggcggccATTTCTTCATAAGGGTAGGAGAG-3'	Full-length *ALG2*
AG11BPfw	5'-tgtaatggccattacggccATGGGCAGTGCTTGGACAAACT-3'	Full-length *ALG11*
AG11BPrv	5'-gcctttggccgaggcggccCCCCTTTCCTCCTCTTCTAATAA-3'	Full-length *ALG11*
SC59BPfw	5'-tgtaatggccattacggccATGGTCGCTATAATACCTCATGCTTCC-3'	*C*-terminally truncated *SEC59*
SC59BP/HR2rv	5'-gcctttggccgaggcggccttATATTTTGTGAATATCAGACCAACCATTA-3'	*C*-terminally truncated *SEC59*
SC59BP/LR2rv	5'-gcctttggccgaggcggccTTATAAGATATATCAGCGGTAACAATG-3'	*C*-terminally truncated *SEC59*
SC59BP/*ΔN106*fw	5'-tgtaatggccattacggccatgTGGCAACATGGTTACAAAAGCCTAC-3'	*N*-terminally truncated *SEC59*
SC59BP/*ΔN118*fw	5'-tgtaatggccattacggccatgACCATTTACAGTTTATATTTACCGTTTATG-3'	*N*-terminally truncated *SEC59*
SC59BPrv	5'-gcctttggccgaggcggccAGAGTAATTAATTTTTCACAAATCATCATAAAT-3'	*N*-terminally truncated *SEC59*
CH8BPfw	5'-tgtaatggccattacggccATGAATAGTACCGCCGCTGCAATAAAT-3'	*C*-terminally truncated *CWH8*
CH8BP/LR4rv	5'-gcctttggccgaggcggccTTTTCTAAGAAGTTTAGATTCTTCCAGG-3'	*C*-terminally truncated *CWH8*
CH8BP/HR3rv	5'-gcctttggccgaggcggccttGTATATCTTCAGAGAGTTATAGGTAAAAC-3'	*C*-terminally truncated *CWH8*

using the YSUS to analyze the physical interaction of yeast and human glycosyltransferases involved in DLO assembly and successfully detected novel physical interactions[15-20),22),24,25)]. In the early stage of DLO assembly, our previous studies demonstrated five interactions: Alg7p/Alg14p, Alg7p/Alg11p, Alg1p/Alg1p, Alg1p/Alg2p and Alg1p/Alg11p[17)]. In addition, we have investigated the physical interaction of dolichol-related enzymes involved in DLO assembly, including dolichol kinase[21),23),26)]. In the recent study, we found out the physical interaction of Alg5p glucosyltransferase with Sec59p and Cwh8p[22)]. Moreover, we also detected the physical interaction of Dpm1p mannosyltransferase with Sec59p and Cwh8p recently (unpublished observation). These findings prompted us to examine whether the three mannosyltransferases (Alg1p, Alg2p and Alg11p) involved in early assembly of DLO also physically interact with the dolichol-related Sec59p and Cwh8p by using the YSUS. In this analysis, Alg1p, Alg2p and Alg11p were used as bait proteins, whereas Sec59p and Cwh8p were used as prey proteins.

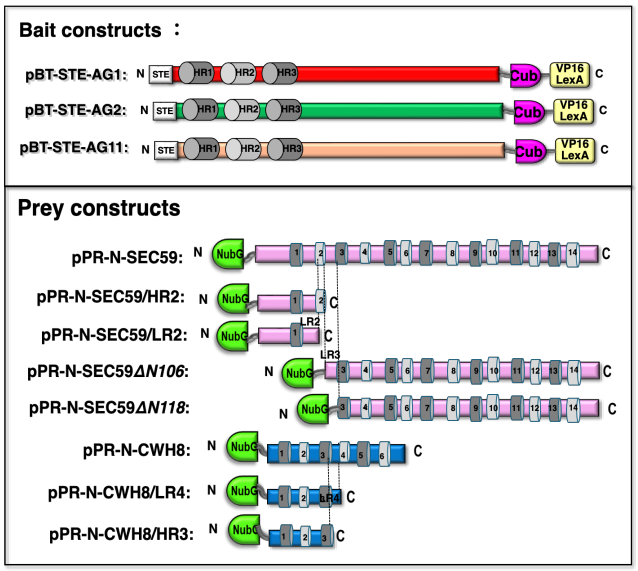

Fig. 2 Plasmid constructs and expressed proteins in this study. Bars and boxes of proteins indicate loop regions (LRs) and hydrophobic regions (HRs), respectively.

2. Experimental Methods

2.1 *Construction of recombinant plasmids for the YSUS*

The coding regions of *ALG1, ALG2 and ALG11* genes were amplified from genomic DNA derived from *Saccharomyces cerevisiae* NMY51 strain by standard PCR method[27)] using each pair of forward and reverse primers listed in Table 1. Each PCR product was then digested with *Sfi* I, purified and ligated to the pBT-STE plasmid vector for expression of each bait protein (Alg1p, Alg2p or Alg11p) which has Cub (*C*-terminal half of ubiquitin protein) tag prepared in the YSUS, at the *C*-terminus. Subsequently, the ligation mix was used for transformation of *Escherichia coli* JM109 strain prepared by SEM method[28)]. Preparation of each recombinant plasmid from the transformants was conducted by standard cloning method[29)], generating pBT-STE-AG1, pBT-STE-AG2 and pBT-STE-AG11 bait constructs (Fig. 2).

For prey constructs for expression of full-length Sec59p and Cwh8p, pPR-N-SEC59, pPR-C-SEC59, pPR-N-CWH8 and pPR-C-CWH8, which were previously prepared, were used in this study (Fig. 2). Moreover, four additional Sec59p prey constructs (pPR-N-SEC59/HR2, pPR-N-SEC59/LR2, pPR-N-SEC59*ΔN106* and pPR-N-SEC59*ΔN118*) and two additional Cwh8p prey constructs (pPR-N-CWH8/LR4 and pPR-N-CWH8/HR3) were also prepared via PCR cloning described above (Fig. 2).

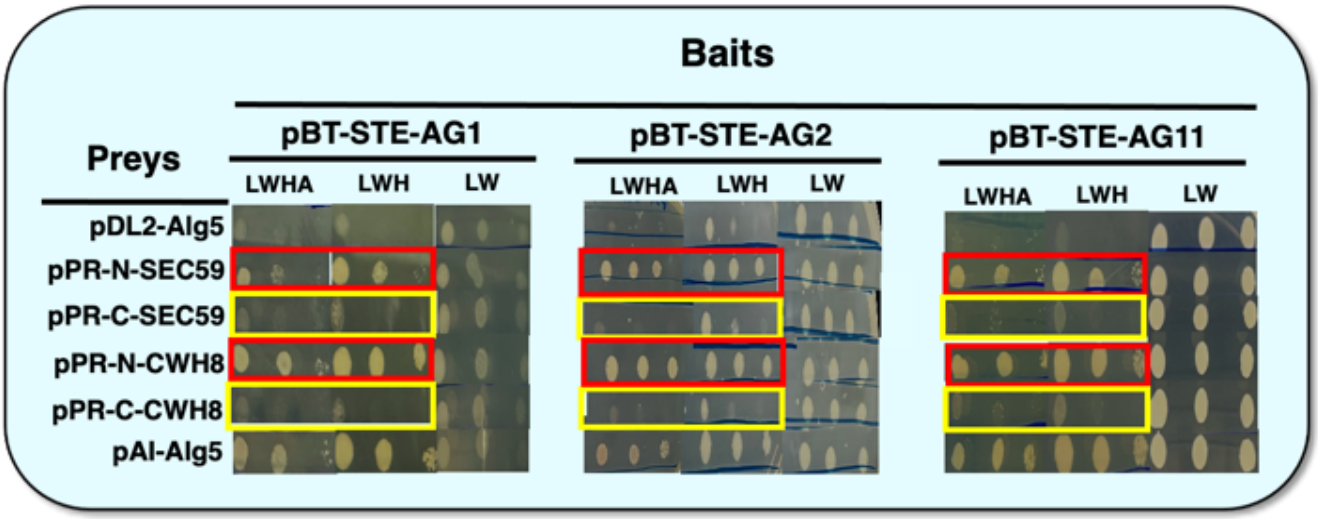

Fig. 3 Growth examination of co-transformants using full-length baits and full-length preys. After the selection of colonies derived from the co-transformants on the SD-LW medium, their suspensions were diluted with sterilized water and adjusted to the OD_{600} values of 1.0, 0.1 and 0.01 (from left to right). These diluents were orderly spotted on the SD-LWH and SD-LWHA media for reporter detection, and SD-LW media for growth control, and then incubated at 30 ºC for 2~4 days. 3-amino-triazole (3-AT) was added to SD-LWH and SD-LWHA media at concentration of 5-10 and 1-2 mM respectively, for preventing background growth due to leaky *HIS3* gene expression.

2.2 *Assays for the physical interaction*

Each bait construct was combined with each prey construct and then they were used for co-transformation of yeast NMY51 strain. After the co-transformation, the co-transformants obtained on the synthetic dextrose (SD) medium lacking leucine and tryptophan (SD-LW) were then subject to the growth examination on the SD medium lacking leucine, tryptophan and histidine (SD-LWH) and SD medium lacking leucine, tryptophan, histidine and adenine (SD-LWHA) according to the manual supplied by Dualsystems Biotech (www.dualsystems.com).

3. Results and Discussion

3.1 *The physical interaction of Alg1p*

In order to test whether Alg1p physically interacts with dolichol-related enzymes, the bait construct pBT-STE-AG1 was combined with each of four prey constructs, pPR-N-SEC59, pPR-C-SEC59, pPR-N-CWH8 and pPR-C-CWH8, and then transformation of the NMY51 cells were conducted. As shown in Fig. 3, co-transformants of pBT-STE-AG1 with pPR-N-SEC59 or pPR-N-CWH8 well grew on SD-LWH and SD-LWHA media (red frame). In contrast, those with pPR-C-SEC59 or pPR-C-CWH8 did not grow on both selective media (yellow frame). These indicate that *C*-terminus of Alg1p might be accessible to both *N*-termini of Sec59p and Cwh8p, but not accessible to both *C*-termini of Sec59p and Cwh8p.

To analyze a region of Sec59p prey with which Alg1p bait would interact, we used two additional Sec59p prey constructs (pPR-N-SEC59/HR2 and pPR-N-SEC59/LR2), which would express truncated Sec59p from the *N*-terminus to the HR2 and that from the *N*-terminus to the LR2, respectively (Fig. 2). In the YSUS analysis, strong or weak interaction could be detected in the form of the growth on both media or only SD-LWH medium, respectively. As a result, co-transformants of pBT-STE-AG1 with pPR-N-SEC/HR2 could grow on both SD-LWH and SD-LWHA media (red frame in Fig. 4A), but those with pPR-N-SEC59/LR2 reduced growth on SD-LWHA medium (orange frame in Fig. 4A). This observation suggests that the HR2 of Sec59p might be associated with the physical interaction with Alg1p.

To analyze a region of Cwg8p prey with which Alg1 bait would interact, we used two additional Cwh8p prey constructs (pPR-N-CWH8/LR4 and pPR-N-CWH8/HR3), which would express truncated Cwh8p from the *N*-terminus to the LR4 and that from the *N*-terminus to the HR3, respectively (Fig. 2). As a result, co-transformants of pBT-STE-AG1 with pPR-N-CWH8/LR4 could grow on both SD-LWH and SD-LWHA media (red frame in Fig. 4A), but those with pPR-N-CWH8/HR3 could not grow on both media (yellow frame in Fig. 4A). This observation indicates that the LR4 of Sec59p might be exclusively critical for the interaction with Alg1p.

3.2 *The physical interaction of Alg2p*

In order to test whether Alg2p physically interacts with dolichol-related enzymes, the bait construct pBT-STE-AG2 was combined with each of four prey constructs, pPR-N-SEC59, pPR-C-SEC59, pPR-N-CWH8 and pPR-C-CWH8, and then transformation of the NMY51 cells were conducted. In growth examination shown in Fig. 3, co-transformants of pBT-STE-AG2 with pPR-N-SEC59 or pPR-N-CWH8 well grew on SD-LWH and SD-LWHA media (red frame) while those with pPR-C-SEC59 or pPR-C-CWH8 did not grow on both selective media (yellow frame). These indicate that *C*-terminus of Alg2p might be accessible to both *N*-termini of Sec59p and Cwh8p, but not accessible to both *C*-termini of Sec59p and Cwh8p.

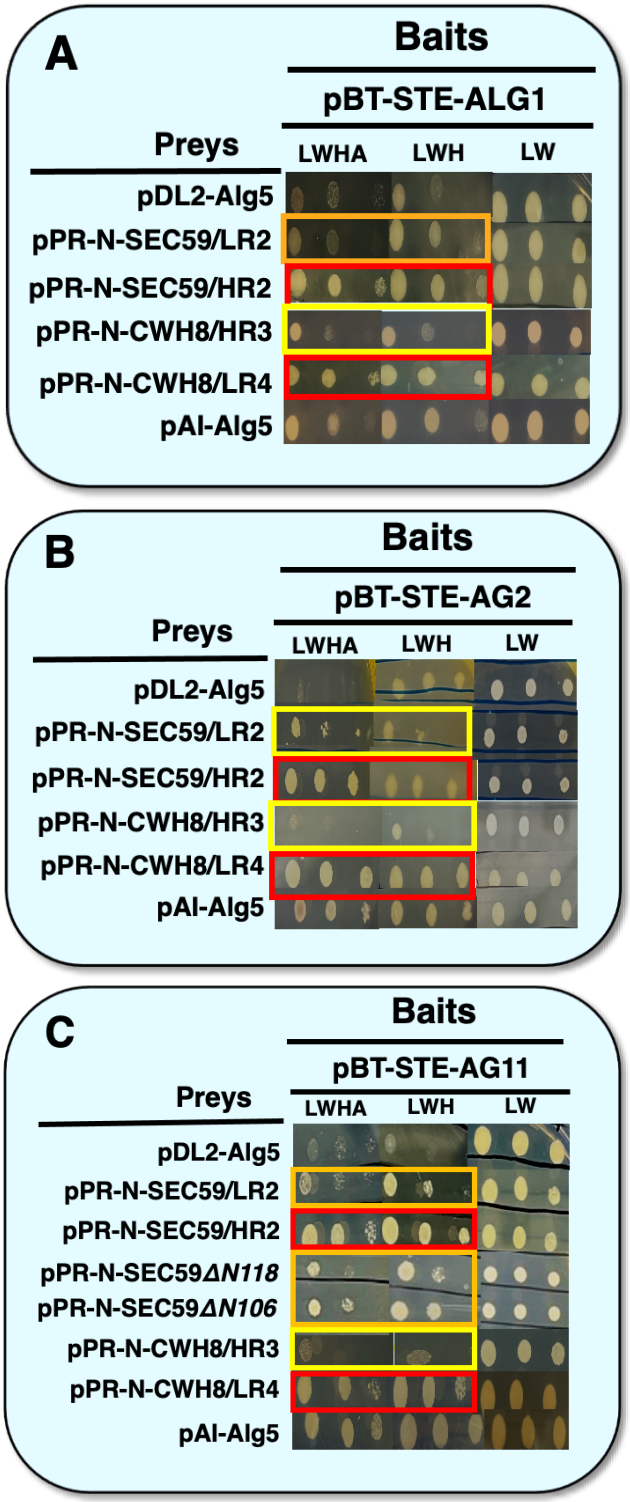

Fig. 4 Growth examination of co-transformants of full-length baits with truncated preys. Each experiment was carried out according to the same procedure as described in the legend of Fig. 3.

To analyze a region of Sec59p prey with which Alg2p bait would interact, we used two additional Sec59p prey constructs (pPR-N-SEC59/HR2 and pPR-N-SEC59/LR2), which would express truncated Sec59p from the *N*-terminus to the HR2 and that from the *N*-terminus to the LR2, respectively (Fig. 2). As a result, co-transformants of pBT-STE-AG2 with pPR-N-SEC59/HR2 could grow on both SD-LWH and SD-LWHA media (red frame in Fig. 4B), but those with pPR-N-SEC59/LR2 could not grow on both media (yellow frame in Fig. 4B). This observation demonstrates that the HR2 of Sec59p might be crucial for the physical interaction with Alg2p.

To analyze a region of Cwg8p prey with which Alg2p bait would interact, we used two additional Cwh8p prey constructs (pPR-N-CWH8/LR4 and pPR-N-CWH8/HR3), which would express truncated Cwh8p from the *N*-terminus to the LR4 and that from the *N*-terminus to the HR3, respectively (Fig. 2). As a result, co-transformants of pBT-STE-AG2 with pPR-N-CWH8/LR4 could grow on both SD-LWH and SD-LWHA media (red frame in Fig. 4B), but those with pPR-N-CWH8/HR3 could not grow on both media (yellow frame in Fig. 4B). This observation means that the LR4 of Sec59p might be essential for the interaction with Alg2p.

3.3 *The physical interaction of Alg11p*

In order to test whether Alg11p physically interacts with dolichol-related enzymes, the bait construct pBT-STE-AG11 was combined with each of four prey constructs, pPR-N-SEC59, pPR-C-SEC59, pPR-N-CWH8 and pPR-C-CWH8, and then transformation of the NMY51 cells were conducted. As shown in Fig. 3, co-transformants of pBT-STE-AG11 with pPR-N-SEC59 or pPR-N-CWH8 well grew on SD-LWH and SD-LWHA media (red frame). In contrast, those with pPR-C-SEC59 or pPR-C-CWH8 did not grow on both selective media (yellow frame). These indicate that *C*-terminus of Alg11p might be accessible to both *N*-termini of Sec59p and Cwh8p, but not accessible to both *C*-termini of Sec59p and Cwh8p.

To analyze a region of Sec59p prey with which Alg11p bait would interact, we used four additional Sec59p prey constructs (pPR-N-SEC59/HR2, pPR-N-SEC59/LR2, pPR-N-SEC59 *Δ N106* and pPR-N-SEC59 *Δ N118*), which would express truncated Sec59p from the *N*-terminus to the HR2, that from the *N*-terminus to the LR2, that from the LR3 to the *C*-terminus and that from the HR3 to the *C*-terminus, respectively (Fig. 2). As a result, co-transformants of pBT-STE-AG11 with pPR-N-SEC59/HR2 could grow on both SD-LWH and SD-LWHA media (red frame in Fig. 4C), but those with pPR-N-SEC59/LR2 reduced growth on SD-LWHA medium (orange frame in Fig. 4C). This observation suggests that the HR2 of Sec59p might be associated with the physical interaction with Alg11p. Co-transformants of pBT-STE-AG11 with pPR-N-SEC59 *Δ N106* or pPR-N-SEC59 *Δ N118* displayed a similar growth pattern of those with pPR-N-SEC59/LR2 (orange frame in Fig. 4C). Taken together, these observations suggest that a region from *N*-terminus to LR2 and another region from HR3 to *C*-terminus of Sec59p might reciprocally collaborate the interaction of the HR2 with Alg11p.

To analyze a region of Cwg8p prey with which Alg11p bait would interact, we used two additional Cwh8p prey constructs (pPR-N-CWH8/LR4 and pPR-N-CWH8/HR3), which would express truncated Cwh8p from the *N*-terminus to the LR4 and that from the *N*-terminus to the HR3, respectively (Fig. 2). As a result, co-transformants of pBT-

STE-AG11 with pPR-N-CWH8/LR4 could grow on both SD-LWH and SD-LWHA media (red frame in Fig. 4C), but those with pPR-N-CWH8/HR3 could not grow on both media (yellow frame in Fig. 4C). This observation indicates that the LR4 of Sec59p might be exclusively critical for the interaction with Alg11p.

4. Conclusion

In order to determine whether the three mannosyltransferases involved in the early assembly of DLO physically interact with two dolichol-related enzymes, we applied the YSUS. The results presented in Fig. 3 clearly demonstrate that Alg1p, Alg2p and Alg11p all interact with both Sec59p and Cwh8p. In addition, the strength of these interactions of the three mannosyltransferases with full-length Sec59p or Cwh8p appear to be equivalent.

To confirm whether this observation is right, we closely investigated these interactions by using truncated Sec59p and Cwh8p. Based on results represented in Fig. 4, it was demonstrated that the LR4 of Cwh8p would be equally critical for three interactions of Alg1p, Alg2p and Alg11p. On the other hand, it appeared that the interaction of Alg2p was more dependent on the HR2 of Sec59p than that of Alg1p or Alg11p.

Biochemical study using co-immunoprecipitation of tagged Alg1p, Alg2p and Alg11p demonstrated that the three mannosyltransferases should form an complex[31], consistent with our previous findings that interactions among Alg1p/Alg1p, Alg1p/Alg2p and Alg1p/Alg11p occur[17]. Therefore, it is estimated that Alg1p or Alg11p might be more easily accessible to Sec59p than Alg2p within this mannosyltransferase complex.

Recently we discovered the interactions between the dolichol kinase and the dolichol pyrophosphatase in human[23] and yeast[32], strongly suggesting that Sec59p and Cwh8p might tightly associated with each other to form a dolichol-related enzymatic complex. Hence, it is possible that the protein interactions detected in this study using the YSUS may reflect the interaction between the mannosyltransferase complex and dolichol-related enzyme complex.

The physical interaction between two membrane enzymes could play a role in positively or negatively altering their enzymatic activities. In this study, we found out that three mannosyltransferases obviously contact with dolichol-related enzymes (Sec59p and Cwh8p) on the rER membrane. This fact raises the possibility that early mannosylation of DLO might be regulated by the status of Sec59p, Cwh8p or Sec59p/Cwh8p complex at protein level. Subsequently, we are now investigating the physical interactions of Sec59p/Cwh8p with glycosyltransferases involved in the late DLO assembly.

References

1) M. Aebi, *N*-linked protein glycosylation in the ER, Biochim. Biophys. Acta Vol.1833, pp.2430-2437 (2013).
2) J. R. Couto, T. C. Huffaker, and P. W. Robbins, Cloning and expression in *Escherichia coli* of a yeast mannosyl-transferase from the asparagine-linked glycosylation pathway, J. Biol. Chem. Vol.259, No.1, pp.378-382 (1984).
3) B. J. Jackson, M. A. Kukuruzinska and P. W. Robbins, Biosynthesis of asparagine-linked oligosaccharides in *Saccharomyces cerevisiae*: the *alg2* mutation, Glycobiology Vol.3, No.4, pp.357-364 (1993).
4) J. F. Cipollo, R. B. Trimble, J. H. Chi, Q. Yan and N. Dean, The yeast *ALG11* gene specifies addition of the terminal alpha 1,2-Man to the $Man_5GlcNAc_2$-PP-dolichol *N*-glycosylation intermediate formed on the cytosolic side of the endoplasmic reticulum. J. Biol. Chem. Vol.276, No.24, pp.21828-21840 (2001).
5) L. Heller, P. Orlean and W. L. Adair Jr., *Saccharomyces cerevisiae* sec59 cells are deficient in dolichol kinase activity, Proc. Natl. Acad. Sci. USA Vol.89, pp.7013-7016 (1999).
6) M. A. van Berkel, M. Rieger, S. te Heesen, A. F. Ram, H. van den Ende, M. Aebi and F. M. Klis, The *Saccharomyces cerevisiae CWH8* gene is required for full levels of dolichol-linked oligosaccharides in the endoplasmic reticulum and for efficient *N*-glycosylation, Glycobiology Vol.9, No.3, pp.243–253 (1990).
7) N. Johnsson and A. Varshavsky, Split ubiquitin as a sensor of protein interactions *in vivo*, Proc. Natl. Acad. Sci. USA Vol.91, No.22, pp.10340-10344 (1994).
8) I. Stagljar, C. Korostensky, N. Johnsson and S. te Heesen, A genetic system based on split-ubiquitin for the analysis of interactions between membrane proteins *in vivo*, Proc. Natl. Acad. Sci. USA Vol.95, pp.5187-5192 (1998).
9) M. Fetchko and I. Stagljar, Application of the split-ubiquitin membrane yeast two-hybrid system to investigate membrane protein interactions, Methods Vol.32, pp.349-362 (2004).
10) S. Thaminy, J. Miller and I. Stagljar, The split-ubiquitin membrane-based yeast two-hybrid system, Methods. Mol. Biol. Vol.261, pp.297–312 (2004).
11) M. Dünnwald, A. Varshavsky and N. Johnsson, Detection of transient *in vivo* interaction between substrate and transporter during protein translocation into the endoplasmic reticulum, Mol. Biol. Cell Vol.10, pp.329-344 (1999).
12) M. J. Massaad and A. Herscovics, Interaction of the endoplasmic reticulum alpha 1, 2-mannosidase Mns1p with Rer1p using the split-ubiquitin system, J, Cell Sci. Vol.114, pp.4629-4635 (2001).
13) W. Scheper, S. Thaminy, S. Kais, I. Stagljar and K. Römisch, Coordination of *N*-glycosylation and protein translocation across the endoplasmic reticulum membrane by Sss1 protein, J. Biol. Chem. Vol.278, No.39, pp.37998-38003 (2003).
14) A. Yan and W. J. Lennarz, Studies on yeast oligosaccharyl transferase subunits using the split-ubiquitin system: Topological features and *in vivo* interactions, Proc. Natl. Acad. Sci. USA Vol.102, No.20, pp.7121-7126 (2005).
15) T. Takahashi and T. Takeuchi, Membrane topological

characterization of the human Alg14 protein, Proc. Schl. Eng. Tokai Univ., Ser. E Vol.44, pp.1-6 (2019).
16) Samantha and T. Takahashi, Analyses of the membrane topology and physical interaction of dolichyl-phosphate-glucose synthase Alg5p, Proc. Schl. Eng. Tokai Univ., Ser. E Vol.49, pp.19-25 (2024).
17) T. Takahashi and X. -D. Gao, Physical interactions among human glycosyltransferases involved in dolichol-linked oligosaccharide biosynthesis, Trends in Glycoscience and Glycotechnology Vol.24, No.136, pp.65-77 (2012).
18) T. Takahashi, N. Yamada and N. Kurimoto, Analyses on the physical interactions of the human dolichyl-phosphate-mannose synthase, Proc. Schl. Eng. Tokai Univ., Ser. J. Vol.57, No.1, pp.5-10 (2017).
19) T. Takahashi, K. Nishimura, N. Maeda and R. Oshiro, Characterization of the membrane topology and physical interaction of human *N*-acetylglucosamine-1-phosphate transferase, Proc. Schl. Eng. Tokai Univ., Ser. E Vol.46, pp.1-6 (2021).
20) T. Takahashi, N. Yamada and R. Oshiro, Characterization of the membrane topology and physical interaction of human dolichol-phosphate-glucose synthase, Proc. Schl. Eng. Tokai Univ., Ser. E Vol.47, pp.1-6 (2022).
21) T. Takahashi, E. Horigome, T. Yamanoto and K. Terajima, Analyses of the membrane topology and physical interaction of human dolichol kinase, Proc. Schl. Eng. Tokai Univ., Ser. E Vol.49, pp.13-18 (2024).
22) Samantha and T. Takahashi, Analyses of the membrane topology and physical interactions of yeast dolichyl-phosphate-glucose synthase Alg5p, Proc. Schl. Eng. Tokai Univ., Ser, E Vol.49, pp.19-25 (2024).
23) K. Terajima, T. Yamamoto, C. Sugimura and T. Takahashi, Analyses of the physical interactions of human dolichol kinase with other dolichol-related enzymes involved in the dolichol cycle, Proc. Schl. Eng. Tokai Univ., Ser, E vol.50, pp.1-6 (2025).
24) Samantha, N. Adachi and T. Takahashi, Analyses of the physical interactions of yeast Alg5p with dolichyl-phosphate-related enzymes in the dolichol cycle, Proc. Schl. Eng. Tokai Univ., Ser, E Vol.50, pp.7-11 (2025).
25) T. Takahashi, T. Miyazaki and K. Sasaki, Characterization of the membrane topology of human chitobiosyl diphospatedolichol beta-1,4-mannosyl-transferase, Proc. Schl. Eng. Tokai Univ., Ser, E Vol.50, pp.13-17 (2025).
26) T. Takahashi, K. Kurihara and Y. Shiraiwa, Characterization of the membrane topology and self-interaction of yeast dolichol kinase Sec59p, Proc. Schl. Eng. Tokai Univ., Ser, E Vol.50, pp.19-23 (2025).
27) H. A. Erlich, PCR Technology, Stockton Press, pp.61-70 (1989).
28) H. Inoue, H. Nojima and H. Okayama, High efficiency transformation of *Escherichia coli* with plasmids, Gene Vol. 96, pp.23–28 (1990).
29) L. Sambrook, E. F. Fritsch and T. Maniatis, Molecular Cloning: A Laboratory Manual. Second edition, Cold Spring Harbor Laboratory Press, NY, (1989).
30) H. Ito, Y. Fukuda, K. Murata and A. Kimura, Transformation of intact yeast cells treated with alkali cations, J. Bacteriol. Vol.153, No.1, pp.163-168 (1983).
31) X. D. Gao, A. Nishikawa and N. Dean, Physical interactions between the Alg1, Alg2, and Alg11 mannosyltransferases of the endoplasmic reticulum, Glycobiology Vol.14, No.6, pp.559-570 (2004).
32) T. Takahashi, M. Terai and K. Yamamoto, Characterization of the membrane topology and physical interaction of yeast Cwh8p, Proc. Schl. Eng. Tokai Univ., Ser. E (*submitted*)

Proc. Schl. Eng. Tokai Univ., Ser. E
51 (2026) 19-25
DOI: 10.18995/24343641. 51. 19

Impacts of Voids within Copper Iodide Hole Transport Layers Prepared via the Ethanol/Iodine Solution Method on Inverted Perovskite Solar Cells

by

Auttaphon PLOYPRADIT*1 and Tetsuya KANEKO*2

(Received on Apr. 15, 2026 and accepted on Jul. 16, 2026)

Abstract

The hole transport layer (HTL) plays a crucial role in perovskite solar cells (PSCs). This study used copper iodide (CuI) as the HTL for inverted planar PSCs. The CuI layer was fabricated from a copper nitride (Cu_3N) thin film by sputtering and iodization using the iodine/ethanol solution method. A power conversion efficiency (PCE) of 2.93% with a short-circuit current density (J_{SC}) of 10.41 mA/cm², an open-circuit voltage (V_{OC}) of 0.58 V, and a fill factor (FF) of 0.47 was achieved in forward scanning using the CuI layer thickness of 539 nm. The results demonstrate that the CuI layer enables device operation in inverted planar PSCs with Ag electrodes. However, a low V_{OC} was obtained due to voids within the CuI layer; these voids allowed the perovskite layer to contact the ITO electrode. In addition, the voids created a larger interface area between the perovskite and CuI layers. Both issues increased carrier recombination and reduced device performance. From this perspective, voids in the CuI HTL prepared via the ethanol/iodine solution method are a critical issue for improving the performance of inverted planar PSCs.

***Keywords*:** Copper iodide, Hole transport layer, Ethanol/iodine solution method, Perovskite solar cell

1. Introduction

In recent years, organic/inorganic hybrid organometal trihalide perovskite solar cells (PSCs) have developed as a focus of research in photovoltaic technology, owing to their enhanced power conversion efficiencies and relatively easy fabrication process[1-3]. Especially, the hole transport layer (HTL) has played an important role in inverted planar PSCs. Inorganic hole-transport materials, such as nickel oxide (NiO_x), copper oxide (Cu_2O), copper thiocyanate (CuSCN), and copper iodide (CuI), have attracted increased attention due to their stability, wide band gaps, and lower cost[4-6]. The p-type semiconductor NiO_x has received special attention as an HTL for the fabrication of inverted planar PSCs due to its high chemical stability and ease of fabrication[7]. Although NiO_x is one of the most widely used inorganic HTLs, its intrinsic conductivity is relatively low. This remains a major limitation. Therefore, dopant engineering is often required. Various dopants, such as Li, Cu, Ag, Cs, Co, Zn, Sr, and rare-earth elements, have been introduced. These dopants are used to improve hole transport, tune the work function, and suppress defects[8-10]. In contrast, CuI exhibits intrinsically high p-type conductivity. As a result, the CuI is considered one of the promising HTLs for efficient hole extraction[11].

The research on the fabrication of the CuI layer has used spin coating for deposition[12]. Other research has reported that the CuI layer fabricated from the copper layer by thermal evaporation, followed by exposure to iodine vapor[13]. Nevertheless, achieving a homogeneous layer fabrication on a large scale through spin coating and gas transformation can be challenging.

In our previous reports, we presented the fabrication method for the CuI layer using an ethanol/iodine solution[14,15]. This method offers a low-cost, scalable fabrication suitable for industrial applications. However, voids formed in the CuI layer after iodization using the ethanol/iodine solution method. The presence of voids in the CuI layer may allow direct contact between the perovskite and ITO layers, thereby increasing carrier recombination and compromising overall device performance[14]. In this work, the impacts of voids within the CuI layer prepared via the ethanol/iodine solution method were investigated. To achieve this, a benchmark NiO thin film was employed to examine direct contact through these voids[16]. The NiO thin film serves as a protective layer between the CuI and ITO layers. In addition, the NiO layer acts as a diagnostic layer by eliminating the direct contact pathway between the perovskite and ITO layers. This allows other issues of the

*1 Graduate Student, Course of Science and Technology
*2 Associate Professor, Department of Electrical and Electronic Engineering

voids to be identified. In particular, the void sidewalls increase the interface area between the perovskite and CuI layers compared with a flat CuI layer, which may also contribute to device degradation. This modification will allow us to assess the impacts of voids in the CuI layer on the performance of inverted planar perovskite solar cells.

2. Experimental Methods

The CuI layers were fabricated from thin films of copper nitride (Cu_3N). The layers were fabricated on glass and glass/indium tin oxide (ITO). The glass substrates were used to characterize the Cu_3N thin film and the CuI layer. The CuI layers were fabricated on glass/ITO substrates for thickness estimation and investigation of the surface morphology. The glass and glass/ITO substrates were cleaned with distilled water, soap solution, isopropyl alcohol (IPA), and acetone, then dried with nitrogen gas and subjected to ultraviolet (UV) treatment. After cleaning the substrates, they were set up for sputtering. The RF magnetron sputtering was used to deposit the Cu_3N thin films. The sputtering conditions were 40 W of power, a 1:1 argon (Ar) and nitrogen (N_2) gas mixture, and a pressure of 1 Pa for 150 min. After the Cu_3N thin films were fabricated, they were immersed in an ethanol/iodine solution at 0.003 mol/L for 60 min to iodize them into the CuI layers. In this work, to understand the effect of voids in the CuI layer, we used a NiO thin film with a thickness of 56 nm as a benchmark. The NiO HTL without doping was fabricated using the RF magnetron sputtering. A sputtering condition of 150 W with 71 SCCM Ar gas for 53 min was used to fabricate the NiO HTL. After fabricating the HTLs, the perovskite solution was prepared and spin-coated onto glass/ITO/CuI, glass/ITO/NiO/CuI, and glass/ITO/NiO. In the next step, the [6,6]-phenyl-C61-butyric acid methyl ester (PCBM) solution was prepared and spin-coated onto the perovskite layer. The perovskite and PCBM solutions were deposited in the glovebox under a nitrogen gas flow to reduce the humidity. Finally, the silver (Ag) electrodes were deposited onto the PCBM and the ITO layers by thermal evaporation. Figure 1 shows the inverted planar PSCs structure using various HTLs in this study.

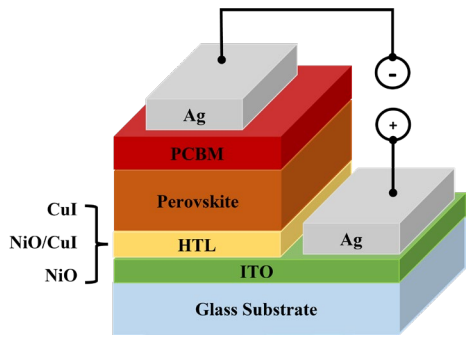

Fig. 1 The inverted planar PSCs structure using various HTLs.

For HTL estimation, a Bruker DekTak stylus profilometer was used to measure the thicknesses of the Cu_3N thin films, the CuI layers, and the benchmark NiO thin film. The four-point probe method was used for the resistivity test. A Hitachi U-4100 spectrophotometer was used to assess the optical characteristics. A solar simulator (100 mW/cm^2, AM 1.5) with an active cell area of 0.03 cm^2 was used to estimate the solar cell performance. The Bunkou Keiki SMI-250JA was used to estimate the incident photon-to-electron conversion efficiency (IPCE). SEM images were also used to investigate the surface morphology of the layers with the JEOL NeoScope JCM-6000 Plus benchtop scanning electron microscope. All estimations were done at room temperature.

3. Results and Discussion

3.1 Hole transport layers

Figure 2 shows the iodization process of the Cu_3N thin films to CuI layers using the ethanol/iodine solution method. The Cu_3N thin film color was dark brown, while the CuI layer was transparent. The different colors of the Cu_3N thin film and the CuI layer indicate that the iodization process for the CuI layer was complete. The Cu_3N thin film with a thickness of 167 nm was obtained upon completion of the sputtering process. After the iodization process was complete, the resulting CuI thin film was approximately three times as thick as the original Cu_3N precursor film. The CuI layer with a thickness of 539 nm and a resistivity of 127 mΩ·cm was obtained.

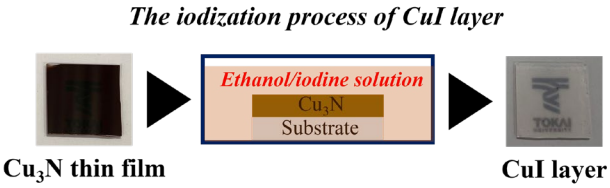

Fig. 2 The iodization process of the Cu_3N thin film to CuI layer using the ethanol/iodine solution method.

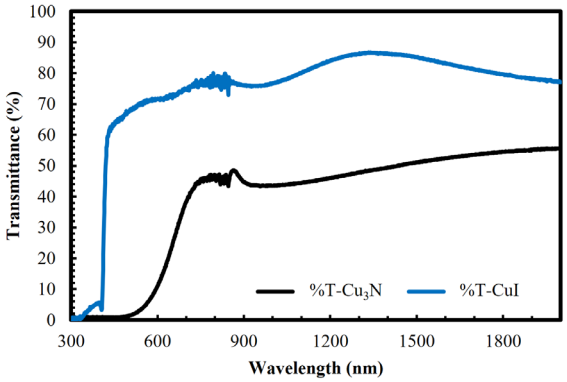

Fig. 3 Transmittance spectra with the diffuse method of the Cu_3N thin film and the CuI layer fabricated onto the glass substrate.

Figure 3 shows the transmittance spectra of the Cu_3N thin film and the CuI layer. Both the Cu_3N thin film and the CuI layer were fabricated on glass substrates. In the

wavelength range of 300 to 600 nm, the transmittance of the Cu_3N thin film was low. After 600 nm, it slowly increases to 45% at 800 nm. In the CuI layer, transmittance in the short wavelength of 300-410 nm range was notably low, indicating strong absorption in this spectral region. Beyond 410 nm, the diffuse transmittance increases to approximately 70% at 500 nm. These findings provide insights into the optical behavior of the CuI layer, particularly its strong absorption at short wavelengths and its increasing transparency in the visible region. This suggests that the CuI layer prepared via the ethanol/iodine solution method is highly transparent. In addition, the excitonic band-edge absorption of CuI is located at ~3.06 eV (~405 nm). The emission features are typically observed around 405–420 nm[17,18]. The CuI layer prepared via the ethanol/iodine solution method also shows an absorption feature around ~400 nm, which corresponds well to the reported excitonic absorption of CuI.

The optical band gap (E_g) was estimated from the optical spectra. Figure 4 shows the Tauc plot of the Cu_3N thin film and the CuI layer. The E_g of 2.9 eV was obtained with the CuI layer, whereas the Cu_3N thin film showed an E_g of 1.4 eV. From these results of the optical spectra and the E_g shown in Figs. 3 and 4, we can conclude that the CuI layers prepared via the ethanol/iodine solution method were successfully fabricated. However, the E_g of 2.9 eV remains lower than the typical E_g of CuI. The typical E_g of the CuI layer was 3.1 eV[19].

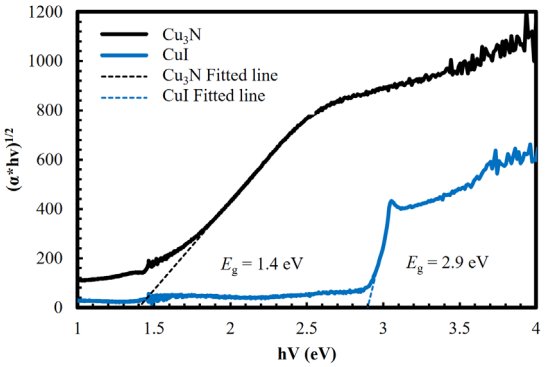

Fig. 4 Optical band gap of the Cu_3N thin film and the CuI layer calculated from the Tauc plot.

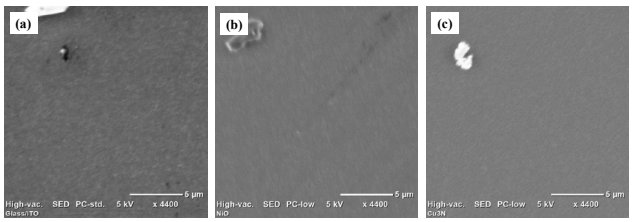

Fig. 5 Top-view SEM images of (a) Glass/ITO, (b) NiO, and (c) Cu_3N.

SEM images were used to study the surface morphology of the layers. Figure 5(a) shows the SEM image of glass/ITO. The flat surface was observed on the ITO surface. Figures 5(b) and 5(c) present SEM images of the NiO and Cu_3N thin films deposited by RF magnetron sputtering. After sputtering, both the NiO and Cu_3N thin films exhibit flat surfaces. The surface morphology of these films is similar to that of the ITO substrate.

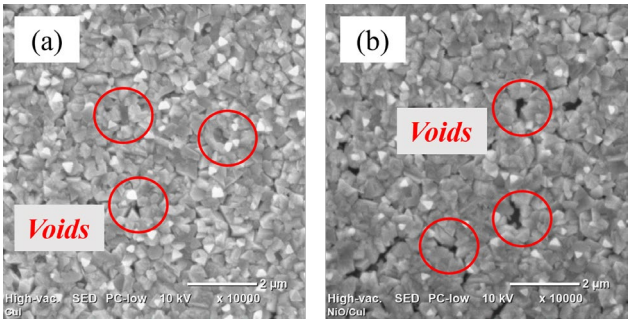

Fig. 6 Top-view SEM images of (a) Glass/ITO/CuI and (b) glass/ITO/NiO/CuI. All images were acquired at a magnification corresponding to a 2 µm scale bar, which differs from the magnification used in Fig. 5.

Figures 6 (a) and (b) illustrate the SEM images of the CuI layers with a magnification corresponding to a 2 µm scale bar, which is different from the magnification used in Fig. 5. In Fig. 6 (a), the CuI layer was fabricated on the ITO surface, and in Fig. 6 (b), the CuI layer was fabricated on the NiO surface. The results demonstrate that voids were obtained in the CuI layers on both the ITO and the NiO surfaces. Voids were observed only on the CuI layer surface. In contrast, no voids were observed on the Cu_3N thin film surface, as shown in Fig. 5(c). These points show that using the ethanol/iodine solution method also yielded voids within the CuI layer[20]. Therefore, the SEM images indicate that the voids within the CuI layer may have formed during its formation by the ethanol/iodine solution. One plausible mechanism for void formation in the CuI layer involves excess immersion in the ethanol/iodine solution. SEM observations reveal that both the density and size of voids increase with increasing iodization time[21]. This finding suggests that excess exposure to the iodine/ethanol solution may partially dissolve the CuI layer. The resulting reduction in film continuity promotes the formation and growth of voids. In particular, thinner CuI layers exhibited a higher void density than thicker layers prepared under the same conditions[14]. In contrast to short-time iodization using the ethanol/iodine solution, the results exhibited significantly fewer voids than those prepared with longer iodization times[21]. The voids in the CuI layers might affect the performance of the perovskite solar cells. In future work, the mechanism of void formation will be investigated in greater detail.

3.2 Perovskite solar cells

Table 1 presents the solar cell parameters of the inverted planar PSCs with various HTLs. Figure 7 shows the current density-voltage (*J-V*) characteristics of the same cells, as summarized in Table 1. This work presents the best cell performances of each HTL layer type. We have achieved

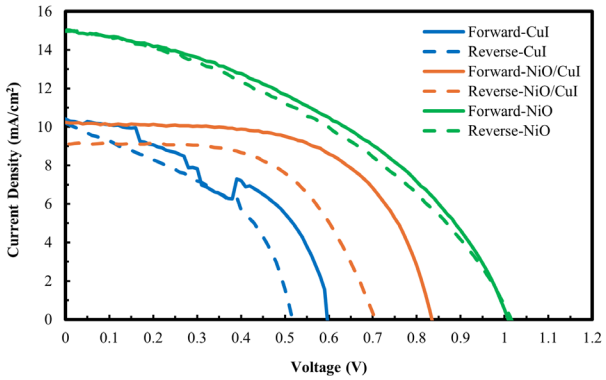

Fig. 7 Current density – voltage (*J-V*) characteristic of the inverted planar PSCs with various HTLs.

a power conversion efficiency (PCE) of 2.93% with a short-circuit current density (J_{SC}) of 10.41 mA/cm^2, an open-circuit voltage (V_{OC}) of 0.58 V, and a fill factor (FF) of 0.47 in forward scanning by using a single CuI HTL. The results demonstrate that the CuI HTL prepared via the ethanol/iodine solution method enables device operation in inverted planar PSCs with Ag electrodes. However, the low performance of the perovskite solar cell using the CuI HTL was obtained. This may be attributed to voids in the CuI layer, as shown in Fig. 6(a). The voids within the CuI layer may allow the perovskite layer to easily contact the ITO electrode, leading to increased recombination loss.

Table 1 Solar cell parameters of the inverted planar PSCs with various HTLs.

HTLs	Scan direction	J_{SC} (mA/cm^2)	V_{OC} (V)	FF	PCE (%)
CuI	Forward	10.41	0.58	0.47	2.93
	Reverse	10.18	0.51	0.46	2.47
NiO/CuI	Forward	10.23	0.83	0.60	5.19
	Reverse	9.13	0.70	0.58	3.80
NiO	Forward	14.97	1.00	0.42	6.38
	Reverse	15.03	1.01	0.39	6.00

When CuI layers with different thicknesses and void densities were applied as HTLs for perovskite solar cell fabrication, the thin CuI layers showed poor solar cell performance. Especially, an extremely low V_{OC} was achieved. In contrast, the thicker CuI layer exhibited an improved V_{OC}. However, strong absorption loss by the thick CuI layer reduced the external quantum efficiency at short wavelengths. These results suggest that both the thickness and void density of the CuI layer negatively impact device performance[14,21]. To confirm this, we used a NiO thin film as a barrier to prevent direct contact between the perovskite layer and the ITO electrode. As summarized in Table 1, incorporating the NiO thin film significantly improved performance. Especially, the V_{OC} parameter significantly increased from 0.58 V to 0.83 V in the forward scan. The V_{OC} improvement is due to the NiO thin film preventing direct contact between the perovskite and ITO layers. Since carrier recombination at the perovskite and ITO interface

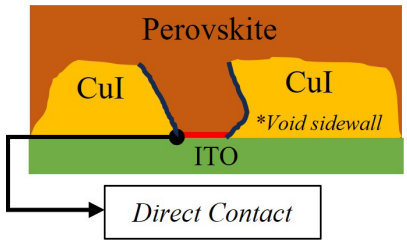

Fig. 8 Cross-section schematic diagram of the direct contact problem between the perovskite and ITO layers through voids within the CuI layer.

was reduced, the solar cell performance improved. To clarify the problems caused by voids within the CuI layer, Fig. 8 illustrates the direct contact problem between the perovskite and ITO layers through voids within the CuI layer.

In the structure with a NiO thin film as a protective layer (NiO/CuI), the FF also improved from 0.47 to 0.60 in the forward scan. However, the V_{OC} remained lower than that of the structure using only the single NiO layer. The reason is that voids were still obtained in the CuI layer even after the insertion of the NiO thin film, as shown in Fig. 6 (b). Remaining voids within the CuI layer may increase the interface area between the perovskite and CuI layers through the void sidewalls. As a result, the effective contact area becomes larger than that of a flat CuI layer. This increased interface area may contribute to device degradation, leading to enhanced carrier recombination and reduced V_{OC}. Moreover, the solar cell with a CuI layer exhibits significant hysteresis. The hysteresis index (HI) was calculated as HI = ($PCE_{reverse}$ − $PCE_{forward}$) / $PCE_{reverse}$[22]. The negative HI values of -0.19 for CuI and -0.37 for NiO/CuI indicate inverted hysteresis. In contrast, the single NiO thin-film device showed a lower inverted hysteresis index of -0.06. Inverted hysteresis means that the forward scan yields a higher PCE than the reverse scan. This inverted hysteresis index behavior is consistent with charge accumulation at the HTL/perovskite interface under forward-bias conditions, arising from unfavorable energy-level alignment and interface-trap states[23]. However, the HI result using the CuI layer is higher than that of a single NiO thin film. A main possible reason is that voids within the CuI layer increased interface trap states, leading to charge accumulation[24,25]. Reducing the void density in the CuI layer suppresses the hysteresis of the perovskite solar cell[26]. These results suggest that voids are a major cause of hysteresis.

Furthermore, energy-level alignment is an important factor affecting solar-cell performance. Previous reports suggest similar valence-band maximum levels, which are expected to yield similar hole-extraction behavior in CuI and NiO[27,28]. In this work, the CuI HTL prepared via the ethanol/iodine solution method contains significant voids. Voids within the CuI layer may cause interface defects and a charge-transport pathway[29]. Figure 9 illustrates the hypothesized energy-level alignment around the CuI HTL. Figure 9(a) presents the hypothesized energy-level alignment for direct contact through the voids within the CuI layer. If the perovskite layer directly contacts the ITO layer

through the voids, no electron-blocking layer is present. As a result, carrier recombination may increase. Figure 9(b) shows the hypothesized energy-level alignment of the perovskite/CuI interface. The reported valence band maximum (E_{VBM}) of CuI is approximately -5.3 eV[27], which is close to the E_{VBM} of NiO at -5.2 eV[28]. Based on the reported E_{VBM}, similar hole-extraction behavior is expected for CuI and NiO. Therefore, CuI can serve as both a hole-transport and an electron-blocking layer as an HTL in PSC, as shown in Fig. 9(b). However, the CuI HTL prepared via the ethanol/iodine solution method contained voids. These voids increased the interface area between the perovskite and CuI layers via the sidewalls of the voids. The enlarged interface may enhance carrier recombination, thereby reducing the V_{OC}. Nevertheless, an idealized band-alignment model may not accurately represent the actual charge extraction in this study. After the void problem within the CuI layer is resolved, investigation of the energy-level alignment will be an important direction for future work. Based on the discussion above, it is clearly understood that voids within the CuI layer are a critical issue and significantly contribute to performance degradation.

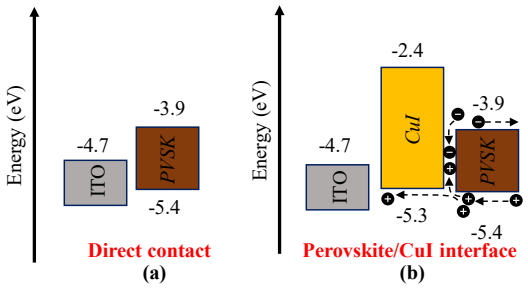

Fig. 9 Schematic illustration of the hypothesized energy-level alignment around the CuI HTL.

In addition, one reason for the low performance in the PSCs with the CuI HTL was the optical loss in the CuI layer. Figure 10 shows the IPCE spectra of the PSCs with various HTLs. In the short wavelength of 300 to 410 nm, the PSCs using the CuI layer and NiO/CuI layers show a low IPCE value compared with the single NiO layer, which may be due to the optical loss of the thick (539 nm) CuI layer.

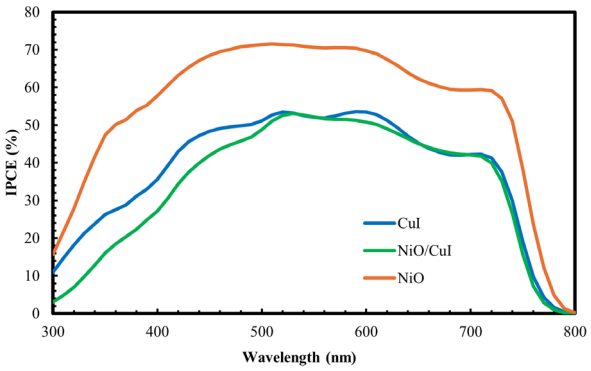

Fig. 10 IPCE spectra of the inverted planar PSCs with various HTLs.

Figure 11 shows the transmittance spectra obtained with the diffuse method for the CuI layer and the NiO thin film fabricated on the glass/ITO substrate. In the short-wavelength region (300–410 nm), the glass/ITO/CuI structure shows a maximum transmittance of 4% at 400 nm. In contrast, glass/ITO/NiO shows 68% at the same wavelength. The low transmittance of the CuI layer is attributed to strong absorption in the thick CuI layers (539 nm). This increases optical loss. The thick CuI HTL prepared using the ethanol/iodine solution method resulted in low IPCE in this wavelength range in inverted planar PSCs. From this point, a thin CuI layer is therefore required to reduce optical loss.

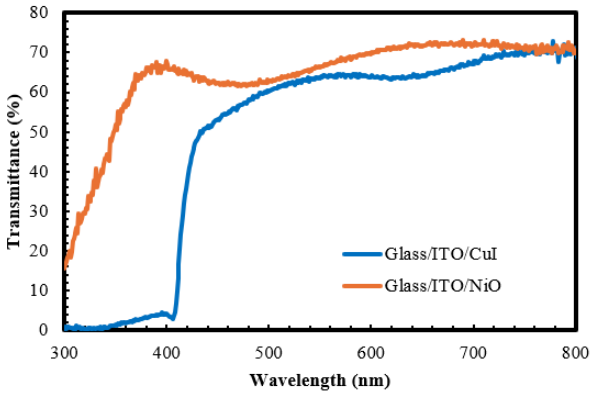

Fig. 11 Transmittance spectra with the diffuse method of the CuI layer and the NiO thin film fabricated onto the glass/ITO substrate.

A significant reduction in IPCE was obtained in PSCs with CuI layers not only in the UV region but also across the entire wavelength range, as shown in Fig. 10. The results suggest that the difficulty of carrier collection caused the low J_{SC} of the cells with CuI layers. The voids within the CuI layer create a large interface area, which may reduce carrier collection. Therefore, the low performance with low V_{OC} and low J_{SC} of PSCs with CuI HTL by the ethanol/iodine solution method can be attributed to the voids within the CuI layer. Therefore, suppressing void formation and achieving a flat CuI surface are critical for improving carrier collection and preventing direct contact. A proposed hypothesis is that void formation occurs during immersion in the ethanol/iodine solution. To address the voids formed during iodization, one possible approach is to optimize the iodine concentration and iodization time. Optimizing the iodization process may improve the CuI morphology and reduce void formation. In addition, post-annealing of the Cu_3N thin film may further improve the morphology of the resulting CuI layer. If these issues can be addressed, CuI HTLs prepared using the ethanol/iodine solution method could serve as a promising approach for achieving high-performance solar cells.

4. Conclusion

In this study, an inverted planar perovskite solar cell employed a CuI HTL prepared by the ethanol/iodine solution method. The CuI thickness of 539 nm was used for inverted planar PSCs. The power conversion efficiency (PCE) of 2.93% with a J_{SC} of 10.41 mA/cm², a V_{OC} of 0.58 V, and a

FF of 0.47 was obtained in the forward scan. The results demonstrate that the CuI HTL prepared via the ethanol/iodine solution method enables device operation in inverted planar PSCs with Ag electrodes. The primary performance limitation is attributed to voids within the CuI layer. The voids within the CuI layer allow direct contact between the perovskite layer and the ITO electrode. The insertion of a NiO thin film as a protection layer helps us to understand this issue. The increase of the V_{OC} from 0.58 V to 0.83 V in the inverted planar PSC results from less recombination at the ITO and perovskite layer interface. However, the PSC with the NiO/CuI HTL still exhibited a low V_{OC}. This was mainly due to remaining voids in the CuI layer. These voids increased the interface area, thereby affecting carrier recombination. From this point of view, solving the voids within the CuI layer is a significant issue to improve the performance of the inverted planar PSCs with CuI HTLs using the ethanol/iodine solution method.

References

1) N. Posopa, A. Sakulkalavek, N. Chanlek, J. Kaewkhao, and R. Sakdanuphab: Room-temperature rapid synthesis of CuI thin films via liquid iodination method, Superlattices and Microstructures Vol. 141, 106501 (2020).
2) W. S. Yang, J. H. Noh, N. J. Jeon, Y. C. Kim, S. Ryu, J. Seo and S. I. Seok: High-performance photovoltaic perovskite layers fabricated through intramolecular exchnge, Science Vol. 348, pp. 1234-1237 (2025).
3) M. Luo, X. Zong, M. Zhao, Z. Sun, Y. Chen, M. Liang, Y. Wu, and S. Xue: Synergistic effect of amide and fluorine of polymers assist stable inverted perovskite solar cells with fill factor > 83%. Chemical Engineering Journal Vol. 442, 136136 (2022).
4) X. Yin, P. Chen, M. Que, Y. Xing, W. Que, C. Niu, and J. Shao: Highly Efficient Flexible Perovskite Solar Cells Using Solution-Derived NiO_x Hole Contacts, ACS Nano Vol. 10, pp. 3630–3636 (2016).
5) C. Zuo and L. Ding: Solution-Processed Cu_2O and CuO as Hole Transport Materials for Efficient Perovskite Solar Cells. Small Vol. 11, pp. 5528−5532 (2015).
6) S. Z. Haider, H. Anwar, and M. Wang: A comprehensive device modelling of perovskite solar cell with inorganic copper iodide as hole transport material, Semicond. Sci. Technol. Vol. 33, 035001 (2018).
7) K. Zhao, Y. Zhao, Y. Tan, K. Hu, and Z.-S. Wang: Boosting the Conductivity of the NiO_x Layer through Cerium Doping for Efficient Planar Inverted Perovskite Solar Cells, ACS Appl. Energy Mater. Vol. 4, pp. 9038–9045 (2021).
8) F. P. Gokdemir Choi, H. Moeini Alishah, and S. Gunes: Cerium and zinc co-doped nickel oxide hole transport layers for gamma-butyrolactone based ambient air fabrication of $CH_3NH_3PbI_3$ perovskite solar cells, Applied Surface Science Vol. 563, 150249 (2021).
9) X. Xia, Y. Jiang, Q. Wan, X. Wang, L. Wang, and F. Li: Lithium and Silver Co-Doped Nickel Oxide Hole-Transporting Layer Boosting the Efficiency and Stability of Inverted Planar Perovskite Solar Cells, ACS Appl. Mater. Interfaces Vol. 10, pp. 44501–44510 (2018).
10) L. Zhang, G. Gao, Z. Jiang, A. Wang, B. Li, B. Xu, and J. Ding: Reducing defects: A review of preparation, doping and surface modification of nickel oxide, Coordination Chemistry Reviews Vol. 534, 216563 (2025).
11) K. Takahashi and Y. Suzuki: Perovskite solar cells with CuI inorganic hole conductor, Jpn. J. Appl. Phys. Vol. 56, 08MC04 (2017).
12) O.V. Aliyaselvam, A.N. Mustafa, M.A. Azam, P. Chelvanathan, M.A. Islam, S. Mahalingam, and F. Arith: Unveiling the prospect of copper iodide as hole transporting layer in perovskite solar cell by selective dopant strategy: A review, Materials Science in Semiconductor Processing Vol. 197, 109679 (2025).
13) H. Wang, Z. Yu, X. Jiang, J. Li, B. Cai, X. Yang, and L. Sun: Efficient and Stable Inverted Planar Perovskite Solar Cells Employing CuI as Hole-Transporting Layer Prepared by Solid–Gas Transformation, Energy Technology Vol. 5, pp. 1836–1843 (2017).
14) B. Mahdy, M. Isomura, and T. Kaneko: Fabrication of inverted planar perovskite solar cells using the iodine/ethanol solution method for copper iodide as a hole transport layer, Jpn. J. Appl. Phys. Vol 62, SK1016 (2023).
15) A. Ploypradit and T. Kanako: Effects of Voids within Copper Iodide Hole Transport Layer for Bonding Fabrication of Perovskite Solar Cells through Hot-Pressing Method, 2024 PVSEC-35 Conf., Numazu, Japan, Th2-P51-29 (2024).
16) A. Ploypradit and T. Kaneko: Effect of Voids Within Copper Iodine Hole Transport Layer Using the Ethanol/Iodine Solution Method in Inverted Planar Perovskite Solar Cells, 2025 32nd International Workshop on Active-Matrix Flatpanel Displays and Devices (AM-FPD), Kyoto, Japan, pp. 14-15 (2025).
17) Z.H. Li, J.X. He, X.H. Lv, L.F. Chi, K.O. Egbo, M. Li, T. Tanaka, Q.X. Guo, K.M. Yu, and C.P. Liu: Optoelectronic properties and ultrafast carrier dynamics of copper iodide thin films, Nat Commun Vol. 13, 6346 (2022).
18) Á. Balog, G. F. Samu, P. V. Kamat, and C. Janáky: Optoelectronic Properties of CuI Photoelectrodes, J. Phys. Chem. Lett. Vol. 10, pp. 259–264 (2019).
19) D. Chen, Y. Wang, Z. Lin, J. Huang, X. Chen, D. Pan, and F. Huang: Growth Strategy and Physical Properties of the High Mobility P-Type CuI Crystal, Crystal Growth & Design Vol. 10, pp. 2057–2060 (2010).
20) R. P. Srivastava, H.-S. Jung, and D.-Y. Khang: Transfer-Printed Cuprous Iodide (CuI) Hole Transporting Layer for Low Temperature Processed Perovskite Solar Cells, Nanomaterials Vol. 12, 1467 (2022).
21) A. Ploypradit and T. Kaneko: Uniformity of copper iodide hole transport layers prepared via ethanol/iodine solution method on inverted planar perovskite solar

cells, Jpn. J. Appl. Phys. Vol 65, 12SP04 (2026).
22) M. Minbashi and E. Yazdani: Comprehensive study of anomalous hysteresis behavior in perovskite-based solar cells, Sci Rep, Vol. 12, 14916 (2022).
23) F. Wu, R. Pathak, K. Chen, G. Wang, B. Bahrami, W. Zhang, and Q. Qian: Inverted Current–Voltage Hysteresis in Perovskite Solar Cells, ACS Energy Lett., Vol. 3, pp. 2457–2460, (2018).
24) R. Singh and M. Parashar: Origin of Hysteresis in Perovskite Solar Cells, in Soft-Matter Thin Film Solar Cells, J. Ren and Z. Kan, Eds., AIP Publishing LLCMelville, New York, pp. 1-1-1–42 (2020).
25) H. Javaid, V. V. Duzhko, and D. Venkataraman: Hole Transport Bilayer for Highly Efficient and Stable Inverted Perovskite Solar Cells, ACS Appl. Energy Mater. Vol. 4, pp. 72–80 (2021).
26) A. Ploypradit and T. Kaneko, to be published: Morphology of Copper Iodine Hole Transport Layers Prepared by the Ethanol/Iodine Solution Method for Inverted Planar Perovskite Solar Cells, 2026 33rd International Workshop on Active-Matrix Flatpanel Displays and Devices (AM-FPD), Kyoto, Japan (2026).
27) T. I. Kim, H.-A. Lee, H.-I. Kwon, and I.-J. Park: Band alignment of γ-phase CuI/high-k Al2O3 heterointerface by X-ray photoelectron spectroscopy, Surfaces and Interfaces, Vol. 46, 104190 (2024).
28) S. Liu, V. P. Biju, Y. Qi, W. Chen, and Z. Liu: Recent progress in the development of high-efficiency inverted perovskite solar cells, NPG Asia Mater, Vol. 15, 27 (2023).
29) G. Seo, D. Lee, S. Heo, M. Seol, Y. Lee, K. Kim, S. H. Kim, J. Lee, D. W. Kwak, H. Y. Cho, J. Park, T. K. Ahn, and M. K. Nazeeruddin: Microscopic Analysis of Inherent Void Passivation in Perovskite Solar Cells, ACS Energy Lett., Vol. 2, pp. 1705–1710 (2017).

The School of Engineering of Tokai University publishes two kinds of Reports: the report written in English (once a year) and the one written in Japanese (once a year).

*　　*　　*

Any requests for this proceedings should be addressed to the Editorial Committee of Procceedings of the School of Engineering Tokai University, 4-1-1, Kitakaname, Hiratsuka-shi, Kanagawa-ken. Japan

September 30, 2026

Attention:
The name of this PROCEEDINGS has been changed from 2018 edition as follows.
「PROCEEDINGS OF THE SCHOOL OF ENGINEERINGS」